SARS-CoV-2 neurotropism-induced anxiety/depression-like behaviors require Microglia activation

Qian Ge [1#], Shan Zhou [2#], Jose Porras [2], Panfeng Fu[4], Ting Wang[4], Jianyang Du[1,3] *, Kun Li[2] *

Author affiliations:
[1] Department of Anatomy and Neurobiology, University of Tennessee Health Science Center, Memphis, TN 38163, USA.
[2] Florida Research and Innovation Center, Cleveland Clinic, Port St. Lucie, FL 34987, USA
[3] Neuroscience Institute, University of Tennessee Health Science Center, Memphis, TN, United States.
[4] Center for Translational Science, Florida International University, Port St. Lucie, FL, 34987, USA

*** Correspondence to:**

Kun Li
Florida Research and Innovation Center,
Cleveland Clinic,
Port St. Lucie, FL 34987, USA
Tel:772-419-2239
E-mail:lik11@ccf.org

Jianyang Du
Department of Anatomy and Neurobiology,
University of Tennessee Health Science Center,
Memphis, TN 38163, USA
Tel: 901-448-3463
E-mail: jdu15@uthsc.edu

Authorship note: [#] Q.G. and S.Z. contributed equally to this work.

KEYWORDS COVID-19, SARS-CoV-2, long COVID, post-acute sequelae of SARS-CoV-2 infection, spike protein, Microglia, Amygdala, neurotropism, anxiety- and depression-like behaviors, synaptic transmission and plasticity.

ABSTRACT -196 words

The coronavirus disease 2019 (COVID-19) pandemic, caused by severe acute respiratory syndrome coronavirus 2 (SARS-CoV-2), has been associated with a wide range of “long COVID” neurological symptoms. However, the mechanisms governing SARS-CoV-2 neurotropism and its effects on long-term behavioral changes remain poorly understood. Using a highly virulent mouse-adapted SARS-CoV-2 strain, denoted as SARS2-N501Y$_{MA30}$, we demonstrated that intranasal inoculation of SARS2-N501Y$_{MA30}$ results in viral dissemination to multiple brain regions, including the

amygdala and hippocampus. Behavioral assays indicated a marked elevation in anxiety- and depression-like behaviors post infection. A comparative analysis of RNA expression profiles disclosed alterations in the post-infected brains. Additionally, we observed dendritic spine remodeling on neurons within the amygdala after infection. Infection with SARS2-N501Y$_{MA30}$ was associated with microglial activation and a subsequent increase in microglia-dependent neuronal activity in the amygdala. Pharmacological inhibition of microglial activity subsequent to viral spike inoculation mitigates microglia-dependent neuronal hyperactivity. Transcriptomic analysis of infected brains revealed the upregulation of inflammatory and cytokine-related pathways, implicating microglia-driven neuroinflammation in the pathogenesis of neuronal hyperactivity and behavioral abnormality. Overall, these data provide critical insights into the neurological consequences of SARS-CoV-2 infection and underscore microglia as a potential therapeutic target for ameliorating virus-induced neurobehavioral abnormalities.

INTRODUCTION:

As of April, 3rd, 2024, the global pandemic of COVID-19 has resulted in 774,954,393 reported cases and 7,040264 confirmed deaths (WHO COVID-19 Dashboard https://data.who.int/dashboards/covid19/deaths?n=c). The death rate and hospital admissions related to COVID-19 have been dramatically reduced as a result of extensive vaccination rollouts and improved treatments. However, a substantial number of patients (10-20%) are experiencing a persistent or newly developed set of symptoms following the acute phase of the illness. This condition is commonly referred to as post-acute sequelae of SARS-CoV-2 infection (1) also known as "long COVID," (1). While PASC initially attracted attention for its severe impact on older adults and those with underlying health concerns, it has since been clear that it may also occur in otherwise healthy young people, and it can develop after even a modest initial infection (2, 3). These long-lasting symptoms may persist for weeks or even months, posing challenges for healthcare providers and necessitating further research and support to address the long-term health consequences of the disease.

Among the enduring symptoms of PASC, neurological manifestations stand out prominently. Symptoms include cognitive difficulties, autonomic dysfunction, extreme fatigue, sleep disturbances, and mental health complications such as anxiety and depression (2, 3). The exact cause of these syndromes remains uncertain and is constantly being studied. Possible factors contributing to these symptoms include viral infection of brain cells, immune-mediated phenomena, coincidental events, or a combination of these factors. In vitro studies have provided clear evidence of SARS-CoV-2 infection in human brain organoids or cell cultures (4, 5) Additionally, several autopsy studies have reported the presence of viral RNA or proteins in the brains of patients who died from COVID-19, suggesting the possibility of SARS-CoV-2 neurotropism in the central nervous system (CNS) (5, 6). The neuromechanism of SARS-CoV-2 is not clearly defined, both a systematic mechanism and direct neurotropism have been proposed (7). Recent studies suggest that SARS-CoV-2 triggered the COVID-19 pandemic, and possesses brain neurotropism primarily through binding to the ACE2 on neurons (5), or through tunneling nanotubes (8). In addition to direct invasion of neuronal cells, the activation of microglia and/or astrocytes might contribute to the onset and progression of neurological disorders through abnormal maintenance of homeostasis, leading to altered neuronal activities, and thus is considered critical in defining the neurological damage and neurological outcome of COVID-19 (9).

As the principal innate immune cells of the brain, microglia form the primary focus of research in the field of neuroimmune disease. Microglia are the most dynamic neural cells found to date (10-12). Their profoundly dynamic processes constantly survey the local microenvironment, monitor neuronal activity (13, 14), and respond to infection and injury by releasing pro-inflammatory molecules and phagocytic clearance of apoptotic cells (15). During a homeostatic situation, secretion of molecules and phagocytosis by microglia likewise maintain synaptic transmission and plasticity (16, 17). In contrast, hyperactive microglia can be pathogenic and are associated with symptoms of psychiatric disorders, including anxiety disorders and major depression (18), which have commonly appeared during the COVID-19 pandemic. The activity of microglia can be

95 modulated by neuronal activity (19-21), suggesting the existence of microglia-neuron
96 crosstalk. Despite the high potential relationship between SARS-CoV-2 infection and
97 the neuroimmune system, the mechanisms by which SARS-CoV-2 infection activates
98 pro-inflammatory microglia regulates microglia-neuron interaction and alters neuronal
99 activity have not been adequately studied.
100
101 Further research is essential to comprehensively unravel the mechanisms underlying
102 PASC and its neurological manifestations, as this knowledge is critical for developing
103 effective management and treatment strategies for affected patients. Mouse models
104 serve as invaluable tools in conducting such studies. Unfortunately, mice are naturally
105 resistant to ancestral SARS-CoV-2 infection due to the low affinity of the viral spike (S)
106 glycoprotein to mouse ACE2 receptors (mACE2) (22, 23). To overcome this limitation,
107 several strategies have been employed to overexpress human ACE2 (hACE2) in mice.
108 These approaches include the delivery of exogenous hACE2 using a replication-
109 deficient adenovirus (Ad5-hACE2) or Adeno-associated Virus (AAV-hACE2), and the
110 generation of K18-hACE2 transgenic mice (24-26). These models have been used to
111 investigate the acute infection of SARS-CoV-2 as well as the neurological
112 consequences (5). However, it should be noted that these models have drawbacks that
113 limit their application in studying long-term PASC after SARS-CoV-2 infection. The
114 former may be incapable of getting a brain infection, whereas the latter may acquire
115 severe artificial multiorgan infections with a high mortality rate, rendering them poor
116 candidates for long-term post-infection behavioral testing.
117
118 A highly virulent mouse-adapted SARS-CoV-2 strain, SARS2-N501Y$_{MA30}$, was
119 successfully isolated through serial passage of a recombinant SARS-CoV-2/spike
120 N501Y virus in BALB/c mice (27). After SARS2-N501Y$_{MA30}$ infection, we observed viral
121 titers, viral genomic RNA (gRNA), and subgenomic RNA (sgRNA) in both the lungs and
122 the brains of C57BL/6 mice, indicating the occurrence of virus infection. Fourteen days
123 after the SARS2-N501Y$_{MA30}$ infection, the mice displayed abnormal anxiety- and
124 depression-like behaviors in multiple behavioral paradigms including the open-field test,
125 elevated plus maze test, tail suspension test, and forced swimming test. Due to the

126 critical role of the amygdala in anxiety and depression-like behaviors in rodents and
127 humans (28), we first examined this region and discovered microglia activation following
128 SARS2-N501Y_{MA30} infection. Furthermore, heightened microglia-dependent neuronal
129 activity in the amygdala was evident upon exposure to the spike protein. Our findings
130 uncover the neurotropic potential of SARS-CoV-2 and its direct link to anxiety- and
131 depression-like behaviors through the activation of microglia-mediated
132 neuroinflammatory pathways. This study sheds valuable insights into the neurological
133 repercussions of SARS-CoV-2 infection and suggests microglia as prospective
134 therapeutic targets for mitigating virus-induced neurobehavioral deficits. Understanding
135 the neurological basis of COVID-19-related neuropsychiatric symptoms is critical for
136 developing effective treatments to reduce the long-term impact of PASC on mental
137 health.
138
139 **MATERIALS AND METHODS**
140 **Mice, virus, and cells**
141 Specific pathogen-free 6-9 weeks male and female Balb/c and C57BL/6 mice were
142 purchased from the Jackson Laboratory. All protocols were approved by the Institutional
143 Animal Care and Use Committees of Cleveland Clinic-Florida Research and Innovation
144 Center (CC-FRIC) and the University of Tennessee Health Science Center (UTHSC).
145 The mouse-adapted SARS-CoV-2-N501Y_{MA30} was provided by Drs. Stanley Perlman
146 and Paul McCray at the University of Iowa, USA (27). The virus was propagated in
147 Calu-3 cells and tittered by plaque assay in VeroE6 cells. Calu-3 cells were maintained
148 in minimal essential medium (MEM) supplemented with 20% fetal bovine serum (FBS),
149 0.1 mM nonessential amino acids (NEAA), 1 mM sodium pyruvate, 2 mM l-glutamine,
150 1% penicillin and streptomycin, and 0.15% $NaHCO_3$ at 37°C in 5% CO_2. Vero E6 cells
151 were grown in Dulbecco's modified Eagle medium (DMEM) supplemented with 10%
152 FBS, 0.1 mM NEAA, 1 mM sodium pyruvate, 2 mM l-glutamine, 1% penicillin and
153 streptomycin, and 0.15% $NaHCO_3$ at 37°C in 5% CO_2.
154
155 **Virus infection and titration.**

156 The research involving SARS-CoV-2 was conducted within the biosafety level 3 (BSL3)
157 Laboratory at CC-FRIC. Balb/c or C57BL/6 mice were gently anesthetized using
158 isoflurane and subsequently intranasally infected with 10^4 FPU of SARS-CoV-2-
159 $N501Y_{MA30}$. Post-infection, daily monitoring and weight measurements of the mice were
160 conducted. Tissues were aseptically collected and dissociated in PBS using disposable
161 homogenizers. The viral preparation or supernatants from lung or brain tissue
162 homogenates were subject to sequential dilution in DMEM. These diluted samples were
163 then introduced to VeroE6 cells in 12-well plates to conduct plaque assays (29). After
164 one hour of incubation, the viral inoculums were removed, and the cells were overlaid
165 with a 1.2% agarose solution supplemented with 4% FBS. After 3-day incubation, the
166 cells were fixed with formaldehyde, and the overlays were meticulously eliminated,
167 facilitating visualization of the resulting plaques through the application of a 0.1% crystal
168 violet stain.
169
170 **Behavioral experiments**
171 C57BL/6 mice aged 6-9 weeks were utilized to investigate behavioral responses using a
172 battery of tests as described in **Fig. 2**. We conducted a well-established behavioral test
173 battery in mice fourteen days after intranasal administration of SARS2-$N501Y_{MA30}$ (10^4
174 PFU/ mouse). See detailed descriptions below.
175
176 **Anxiety-like behaviors**

177 ***Open Field Test*** Assessed exploratory and anxiety behaviors in an open-field box for 6
178 minutes. The Open Field task was used to determine the general activity levels, gross
179 locomotor activity, exploration habits of the mice, and anxiety-like behaviors. The
180 evaluation occurred within a cubic, white plastic enclosure measuring 30 cm × 30 cm ×
181 30 cm. Mice were introduced to a corner of the arena and given 6 minutes to acclimate
182 to the unfamiliar surroundings. Their activities were recorded via video. Subsequently,
183 the recorded footage, encompassing metrics such as distance traversed, velocity,
184 resting intervals, movement duration, and time spent in both the center and corners of
185 the arena, was analyzed utilizing Anymaze software. This examination serves as an

186 initial assessment of locomotor activity and anxiety-related behaviors, particularly
187 focusing on the duration spent in the central area.

188 ***Elevated Plus Maze Test*** Evaluated anxiety-like behavior by recording entries into and
189 time spent in the open arms of a maze for 6 minutes. It was conducted as previously
190 described (30). The EPM apparatus, 40 cm high from the floor, consists of two open
191 arms (35 × 10 cm) and two closed arms (35 × 10 cm), those two parts stretch
192 perpendicular to each other and connect in a center platform (5 cm). Mice were placed
193 in the center zone facing an open arm and allowed to explore the maze freely for 6
194 minutes. The time spent in open arms, closed arms, and behaviors of head dipping,
195 sniffing, and grooming were analyzed.
196
197 **Anxiety-like behaviors**

198 ***Tail Suspension Test*** Conduct the tail suspension test to assess depression-like
199 behaviors. Suspend the mice by their tails for 6 minutes using adhesive tape in a
200 controlled environment. Record and analyze the duration of immobility during the
201 predetermined time period (6 minutes). The state of immobility is defined by the
202 absence of movement. The detection of immobility time in these tests serves as a
203 behavioral measure to evaluate the impact of various interventions, such as drug
204 treatments or genetic manipulations, on the animal's response to stress or despair.

205 ***Forced Swimming Test*** Conduct the forced swimming test to assess depression-like
206 behavior. Place the mice individually in a water-filled container for 6 minutes and record
207 their swimming and immobility behaviors. Manually analyze the behavioral results by
208 determining the immobility time for each mouse. Compile the data and calculate the
209 mean immobility time for each experimental group.
210
211 **Bulk RNA sequencing**
212 C57BL/6J mice were intranasally (i.n.) infected with 10^4 FPU of SARS-CoV-2-
213 $N501Y_{MA30}$, as described previously. At specified time points post-infection, whole
214 brains were harvested for RNA extraction using the RNeasy Lipid Tissue Mini Kit

215 (74804, Qiagen, Hilden, Germany). RNA concentration and purity were determined by
216 NanoDrop 2000 spectrophotometer (Thermo Fisher Scientific, Wilmington, DE, USA).
217 Library preparation was performed with the Illumina Stranded mRNA Prep Kit
218 (20040532, Illumina, San Diego, CA, USA), adhering to the manufacturer's instructions.
219 Sequencing was executed on the DNBSEQ-G400 platform (Innomics Inc. Cambridge,
220 MA, USA). Data analysis and visualization was conducted on the Dr. Tom online
221 analysis platform, utilizing the following pipeline: 1. Data Cleaning: Sequencing data
222 was filtered with SOAPnuke, yielding clean reads stored in FASTQ format. 2. Alignment:
223 Clean reads were aligned to the reference genome using HISAT2. 3. Fusion Gene
224 Detection: Ericscript (0.5.5-5) was employed to identify fusion genes. 4. Differential
225 Splicing Gene (DSG) Analysis: rMATS (v4.1.1) was utilized for detecting DSGs. 5. Gene
226 Set Alignment: Bowtie2 aligned the clean reads to the gene set. 6. Expression
227 Quantification: RSEM (v1.2.28) calculated gene expression levels, providing read count,
228 FPKM, and TPM metrics.7. Differential Expression Gene (DEG) Analysis: DESeq2
229 conducted DEG analysis, with a significance threshold set at Q value $\leqslant$ 0.05. 8.
230 Visualization: A heatmap of DEGs was generated using Pheatmap, based on the DEG
231 analysis results. 9. Phenotypic Insight: GO (Gene Ontology, http://www.geneontology
232 .org/) and KEGG (Kyoto Encyclopedia of Genes and Genomes, https://www.kegg.jp/)
233 enrichment analyses of annotated DEGs were performed using Phyper, based on the
234 Hypergeometric test. Significance levels of terms and pathways were adjusted by Q
235 value, with a stringent cutoff (Q value $\leqslant$ 0.05).
236
237 **Quantitative real-time PCR analysis of viral RNA.**
238 Total cellular RNA was isolated using the Direct-zol RNA miniprep kit (Zymo Research,
239 Irvine, CA) following the manufacturer’s protocol including a DNase treatment step.
240 Total RNA (200 ng) was used as the template for first-strand cDNA synthesis. The
241 resulting cDNA was used to quantify the SARS-CoV-2 RNA levels by real-time
242 quantitative PCR using Power SYBR green PCR master mix (Applied Biosystems,
243 Waltham, MA). Average values from duplicates of each sample were used to calculate
244 the viral RNA level relative to the GAPDH gene and presented as $2^{-\Delta CT}$, as indicated
245 (where CT is the threshold cycle). CT values of gRNA and sgRNA from uninfected mice

246 (0 dpi) are constantly > 35. The sequences of the primers used are listed in the **S1**
247 **Table**.
248
249 **Brain slice preparation, S1 protein perfusion, and fEPSP recordings.**
250 Mice were euthanized with overdosed isoflurane and whole brains were dissected into
251 pre-oxygenated (5% CO_2 and 95% O_2) ice-cold high sucrose dissection solution
252 containing (in mM): 205 sucrose, 5 KCl, 1.25 NaH_2PO_4, 5 $MgSO_4$, 26 $NaHCO_3$, 1 $CaCl_2$,
253 and 25 Glucose and sliced into 300 μm on a Leica VT1000S vibratome (31). The
254 transverse amygdala slices were then transferred into the normal artificial cerebrospinal
255 fluid (ACSF) containing (in mM): 115 NaCl, 2.5 KCl, 2 $CaCl_2$, 1 $MgCl_2$, 1.25 NaH_2PO_4,
256 11 glucose, 25 $NaHCO_3$, bubbled with 95% O_2/5% CO_2, pH 7.35 at 20°C-22°C. Slices
257 were incubated in the ACSF at least 1 hour before recording. Individual slices were
258 transferred to a submersion-recording chamber and were continuously perfused with
259 the 5% CO_2/95% O_2 solution (~3.0 ml/min) at room temperature (20°C - 22°C). The
260 spike protein (BPSbIoscience, #510333) was diluted to 167 ng/ml and perfused to the
261 brain slices in the ACSF. For the field EPSP (fEPSP) experiments, neurons were held in
262 current-clamp mode with a pipette solution containing (in mM): 2 KCl (mOsm = 290,
263 adjusted to pH 7.25 with KOH). A concentric bipolar stimulating electrode (FHC Inc.,
264 Bowdoin, ME) was positioned in the cortical inputs in the amygdala slices. Away from
265 the stimulating electrode around 400 μm is a glass recording electrode. EPSPs were
266 recorded in current-clamp mode every 20 seconds and continuously recorded the
267 EPSPs for at least 1 hour. Data were acquired at 10 kHz using Multiclamp 700B and
268 pClamp 10.
269
270 **ATP measurement**
271 Brains were removed from the skull and dissected. Brain slices were then placed in 200
272 μl ice-cold PBS, in the presence of vehicle or spike protein (167 ng/ml, BPS BIoscience,
273 #510333) for the indicated time (10, 30, 60 minutes). To quantify ATP released from the
274 brain slice, we employed an ATP Determination kit (Invitrogen, A22066). Briefly, a 100
275 μl reaction mixture was added to the 96-well cell culture plate, which contains a 10 μl
276 sample or standard solution. After 15 minutes of incubation in the dark, the plate was

277 read using a Synergy Neo2 hybrid multimode microplate reader (BioTek, Winooski, VT,
278 USA). ATP concentrations were determined by reference to a standard curve.
279
280 **Histology.**
281 Tissues (lungs, brain) were collected and fixed in zinc formalin. Following fixation, the
282 lungs were processed for paraffin embedding and sliced into a 4 μm section and the
283 brain was sectioned into 30 μm by a vibratome for subsequent hematoxylin and eosin
284 (H&E) staining by Immunohistochemistry Core of Cleveland Clinic Lerner Research
285 Institute and Immunohistochemistry Core at the University of Tennessee Health Science
286 Center. We have used two serial lung sections (six fields/section) from each animal and
287 a total of 4 to 5 animals per group. Acute lung injury severity was evaluated with ATS
288 guidelines (32) for neutrophil infiltration in alveolar and interstitial space, hyaline
289 membranes, alveolar wall thickening, and proteinaceous debris deposition. Briefly, a
290 scoring system (0-2) was employed for each of the criteria mentioned. An average
291 score of 0 indicated absence of injury, 1 indicated mild to moderate injury, and 2
292 indicated severe injury.
293
294 **Immunohistochemistry**
295 Following the behavioral procedures indicated in the text and figures, the mice were
296 euthanized with overdosed isoflurane and were fixed in Zinc Formalin. Following
297 fixation, we used a vibratome (Leica VT-1000S) to dissect 30 μm amygdala coronal
298 slices, which were collected in ice-cold PBS. To complete immunofluorescence staining,
299 slices were placed in Superblock solution (Thermo Fisher Scientific) plus 0.2% Triton X-
300 100 for 1 hour and incubated with primary antibodies (1:1000 dilution) at 4°C for 24
301 hours (31). Primary antibodies we used include mouse monoclonal antibody to dsRNA
302 (Millipore Cat# MABE1134); Rabbit polyclonal to Iba1 (Abcam Cat# ab108539); Rabbit
303 polyclonal to GFAP (Abcam Cat# ab7260) and mouse anti-NeuN (Cell Signaling Cat#
304 24307). We then washed and incubated slices for one hour with secondary antibodies
305 diluted at a ratio of 1:200 (Alexa Fluor 488 goat anti-rabbit IgG (H+L) (Thermo Fisher
306 Scientific Cat# A-11008); Alexa Fluor 594 goat anti-mouse IgG (H+L) (Thermo Fisher
307 Scientific Cat# A-11032); Alexa Fluor 647 goat anti-mouse IgG (H+L) (Thermo Fisher

308 Scientific Cat# A-21235). VectaShield H-1500 (Vector Laboratories Cat# H-1500) was
309 used to mount slices, while regular fluorescent DIC microscopy and confocal
310 microscopy were used to image the slices.
311
312 For SARS-CoV-2 antigen detection, tissue slides underwent a series of incubation
313 steps. Initially, slides were treated with a blocking reagent (10% normal goat serum) for
314 30 minutes to reduce non-specific binding. Subsequently, a rabbit polyclonal antibody
315 against the SARS-CoV-2 nucleocapsid protein (dilution: 1:4,000, catalog number:
316 40143-T62, Sino Biological) was applied to the slides for 15 minutes. Following the
317 primary antibody incubation, slides were further incubated with Rabbit Envision (Dako)
318 and diaminobenzidine (Dako) as a chromogen to visualize the antigen-antibody
319 complexes.
320
321 **Dendrites and spine morphologic analyses.**
322 After their behavioral testing, we measured the density of dendritic spines on amygdala
323 neurons by using Golgi staining (n = 5 per group). Mice brains were collected, fixed, and
324 processed for the Golgi staining according to the protocol provided by the FD Rapid
325 Golgi Stain Kit (PK401, FD NeuroTechnologies). All images were deconvolved within
326 the Zeiss Application Suite software. The number of dendritic spines was analyzed
327 using plug-in SpineJ as described (33), with modifications. Spines were examined on
328 dendrites of amygdala neurons that satisfied the following criteria: (1) presence of
329 untruncated dendrites, (2) dark and consistent Golgi staining throughout all dendrites,
330 and (3) visual separability from neighboring neurons. We counted the number of
331 dendritic spines along the second dendritic branch at distances from 50 to 100 μm from
332 the soma, in images obtained at 630× magnification. For each neuron, three to five
333 dendritic segments 10 μm in length were analyzed. For each group, 6-10 neurons/mice
334 were analyzed. We used ImageJ software to analyze spines. The analysis of dendritic
335 spines includes the number of spines and spine density, which are critical indicators of
336 synaptic function (34, 35). Spines were classified as thin if they had a long, slender neck
337 and small, Spine length > 0.5 μm; Head perimeter = 2 μm to 3 μm; mushroom, if they
338 had a well-defined, thick neck and spine length > 0.5 μm; Head perimeter ≥ 3 μm; or

339 stubby, if they were short and thick, without a distinguishable neck, spine length ≤ 0.5
340 μm; or filopodia if they were long and curved, spine length > 0.5 μm, head perimeter ≤ 2
341 μm.
342
343 **Statistical analysis.**
344 One-way ANOVA and Tukey's post-hoc multiple comparison tests were used for
345 statistical comparison of groups. An unpaired Student's t-test was used to compare
346 results between the two groups. $p < 0.05$ was considered statistically significant, and we
347 did not exclude potential outliers from our data except the ones that did not receive
348 successful aversive conditioning. The graphing and statistical analysis software
349 GraphPad Prism 8 was used to analyze statistical data, which was presented as means
350 ± SEM. Sample sizes (n) are indicated in the figure legends, and data are reported as
351 biological replicates (data from different mice, and different brain slices). Each group
352 contained tissues pooled from 4-5 mice. Due to variable behavior within groups, we
353 used sample sizes of 10-16 mice per experimental group as we previously described in
354 earlier experiments (31). In behavioral studies, we typically studied groups with five
355 randomly assigned animals per group. The experiments were repeated with another set
356 of four animals until we reached the target number of experimental mice per group.
357
358 **RESULTS**

359 **Neuroinvasion following Respiratory Infection of SARS-CoV-2**

360 The inherent low affinity of the ancestral viral spike (S) glycoprotein for mouse ACE2
361 (mACE2) renders mice naturally resistant to SARS-CoV-2 infection (22, 23). However,
362 specific mutations in the viral spike protein, such as Q498Y, P499T, and N501Y, can
363 enhance binding to mACE2, resulting in asymptomatic infection in mice (36). Through
364 serial passages of a recombinant SARS-CoV-2/spike N501Y virus in BALB/c mice, we
365 successfully isolated a highly virulent mouse-adapted SARS-CoV-2 strain, designated
366 as SARS2-N501Y_{MA30} (27). Interestingly, young C57BL/6 mice exhibited reduced
367 sensitivity to symptomatic infection by SARS2-N501Y_{MA30} **(Fig. 1A)**, making them an
368 optimal model for studying the long-term repercussions of COVID-19. Thus, we
369 intranasally infected mice with 10^4 PFU/mouse of SARS2-N501Y_{MA30} (27). Comparable

370 to our previous findings, young Balb/c mice developed lethal disease, whereas young
371 C57BL/6 mice only displayed minimal weight loss of less than 20% and swift recovery
372 within approximately one week **(Fig. 1B, C)**. In C57BL/6 mice, viral titers peaked at 2
373 days post infection (dpi) in the lungs, followed by the presence of viral titers in the brain
374 peaking at 4 dpi **(Fig. 1D, E)**. Consistent with the observation, both viral genomic RNA
375 (gRNA) and subgenomic RNA (sgRNA) were identified in the lung **(Supplemental**
376 **Fig.1)** and brain **(Fig. 1F, G)**. Immunofluorescence targeting double-stranded RNA
377 (dsRNA) further validated virus RNA replication presence in amygdala brain slices at 4
378 dpi, which subsequently disappeared by 14 dpi. **(Fig. 1H-J)**, with similar observations in
379 the prefrontal cortex (PFC), albeit with slight distinctions **(Fig. 1K)**. These results
380 collectively suggest direct viral infiltration into the brain, alongside respiratory infection.
381 Remarkably, the production of infectious SARS-CoV-2 appeared to be controlled in the
382 brain, as the titer is extremely low **(Fig 1E)** and it did not induce major pathological
383 changes within brain tissues **(Supplemental Fig. 2)**. Further investigation revealed that
384 SARS-CoV-2 replication was predominant in neuron cells in the amygdala, rather than
385 in microglia or astrocytes **(Fig. 1L-N).** These findings indicated a SARS2-N501Y_{MA30}
386 neuroinvasion with a peak at 4 dpi followed by a quick clearance.
387
388 Histological analysis of lung samples revealed acute lung injury using American
389 Thoracic Society (ATS) guidelines for experimental acute lung injury (ALI) based on
390 neutrophil infiltration in alveolar and interstitial space, hyaline membranes, alveolar wall
391 thickening, and proteinaceous debris deposition (32). SARS-CoV-2 infection induced
392 mild lung injury which peaked on day 6, accompanied by viral antigen presence at 2 dpi
393 and disappeared after 6 dpi **(Supplemental Fig 3)**. However, these changes, including
394 infiltration and viral presence, resolved after a 14-week period. To explore host defense
395 responses in SARS-CoV-2-infected mice, we assessed cytokine/chemokine gene
396 expression in the lungs **(Supplemental Fig 1)**. Notably, these genes exhibited
397 significant upregulation at 2 dpi or 4 dpi, gradually subsiding to baseline levels after 6
398 dpi. These findings collectively illustrate a mild respiratory disease in the infected mice,
399 which subsequently resolved within 14 days post-infection.
400

401 **SARS2-N501Y$_{MA30}$ infection induces significant changes in anxiety- and**
402 **depression-like behaviors.**
403 Our investigation successfully detected viral dsRNA within the amygdala **(Fig. 1K)**, an
404 area pivotal in coordinating defensive responses in mice (37) and emotional behaviors
405 in humans (28). This finding prompted us to postulate that the infection may still exert
406 influence over the functionality of this region and consequently modify the defensive
407 behaviors of infected mice. To evaluate the impact of SARS-CoV-2 infection on anxiety-
408 and depression-like behaviors, we conducted a well-established behavioral test battery
409 in mice fourteen days after intranasal administration of SARS2-N501Y$_{MA30}$ (10^4 PFU/
410 mouse) **(Fig. 2A)**. We chose the 14-day time point for behavioral testing since viral
411 infections were observed to have cleared by then. C57BL/6 mice typically recovered
412 from symptomatic infection at 10^4 PFU/mouse within about a week **(Fig. 1B)**. Additional
413 indicators, such as body temperature, fur condition, daily food, and water intake over
414 time (daily records), and mouse locomotion behavior, were similar to those of mock-
415 infected mice at 14 dpi.
416
417 In the open-field test, the infected mice exhibited a decreased duration spent in the
418 center area compared to the mock infection group, indicative of heightened anxiety-like
419 behaviors **(Fig. 2B, left)**. Remarkably, both the SARS2-N501Y$_{MA30}$ and mock infection
420 groups demonstrated similar locomotor activity, implying a complete recovery of
421 locomotion post-infection **(Fig. 2B, right)**. In the elevated plus-maze test, mice in the
422 infected group significantly reduced their time spent in the open arms **(Fig. 2C, left)**,
423 while the number of entries into the open arms remained unaltered **(Fig. 2C, right)**,
424 further substantiating an augmentation in anxiety-like behaviors. Consistent outcomes
425 were observed in the tail suspension and forced swimming tests, both are widely used
426 for evaluating depression-like behaviors, where mice in the virus-infected groups
427 displayed increased immobile time compared to the vehicle groups **(Fig. 2D, E)**. These
428 findings substantiate our conclusion that SARS2-N501Y$_{MA30}$ infection leads to an
429 escalation in anxiety- and depression-like behaviors in mice, indicating potential
430 repercussions on brain function that warrant further exploration.
431

432 **Temporal Gene Signatures in the Brain after SARS-CoV-2 Infection**
433 To further elucidate the molecular mechanisms associated with the observed
434 neuroinvasion and subsequent behavioral alterations, we investigated the temporal
435 dynamics of host transcriptional responses in the brain. This was achieved through bulk
436 RNA sequencing (RNA-seq) on total brain RNA from both mock-infected animal cohorts
437 (0 dpi) and animals infected with SARS2-N501Y_{MA30} at 4 dpi, and 14 dpi, respectively
438 **(Fig. 3 and Supplemental Fig. 4)**. Principal component analysis (PCA) unveiled distinct
439 differences among mock and infected groups with samples from both 4 and 14 dpi
440 **(Supplemental Fig. 4A).** The volcano map of differentially expressed genes (DEGs)
441 revealed significant changes in host genes compared to mock-infected animals or
442 between 4 and 14 dpi based on |log2fold| $\geqslant$ 1.5, Q value $\leqslant$ 0.05 **(Supplemental Fig.**
443 **4B)**. In the 4 dpi vs 0 dpi group, 124 genes were upregulated and 6 were
444 downregulated, while in the 14 dpi vs 0 dpi group, 29 genes were upregulated and 2
445 were downregulated **(Fig. 3A)**. There were only 8 genes upregulated and 5
446 downregulated between 4 and 14 dpi. Notably, 29 upregulated genes in the 14 dpi
447 group also appeared in the 4 dpi group, many of which were associated with synaptic
448 transmission and neuronal development **(Fig. 3B and Supplemental Fig. 4).** Overall,
449 there were 140 genes significantly changed **(Supplemental Fig. 4).**
450
451 We performed pathway analysis based on the Kyoto Encyclopedia of Genes and
452 Genomes (KEGG; http://www.genome.jp/kegg/) and Gene Ontology (GO) based
453 enrichment analysis on the 140 genes **(Supplementary Fig. 4C, E).** Among them, 36
454 genes were implicated to be involved in different neuronal functions in the brain **(Fig.**
455 **3C),** such as synaptic transmission, including Car8, Gabra6, Pcp2, Slc5a1, Tfap2a, or
456 neuronal development, such as Barhl2, Hoxa5, Ppp1r17, Skor1, Fat2, and Nrk. We
457 conducted a KEGG network analysis to delineate the interconnections among the 36
458 identified genes and identified genes related to synaptic vesicle cycle (slc6a2, slc6a4,
459 and slc6a5), long-term depression (Ppp1r17 and Grid2), and neuroactive ligand-
460 receptor interaction (Grid2, Glra1, and Gabra6) **(Fig. 3D).** In conclusion, our
461 comprehensive RNA-seq analysis has unveiled significant changes in host gene
462 expression following viral infection. These alterations suggest a reprogramming of

463 neuronal transcriptional states, corroborating the observed behavioral modifications.
464 Moreover, the data indicate a profound influence on synaptic function and
465 neurodevelopmental processes, underscoring the far-reaching effects of SARS-CoV-2
466 on the central nervous system.
467
468 **SARS2-N501Y$_{MA30}$ infection induces spine remodeling in the amygdala.**
469 To complement the gene expression changes revealed by our RNA-seq analysis, we
470 next examined the morphological alterations in neurons within the amygdala, a region
471 implicated in depression-related behaviors. This investigation aimed to confirm the
472 impact of SARS2-N501Y$_{MA30}$ infection on synaptic plasticity through the observation of
473 dendritic spine remodeling. Dendritic morphology has been widely implicated in the
474 mechanisms governing synaptic plasticity (35, 38, 39). Dendritic spines constitute the
475 principal target of neurotransmission input within the CNS (40), and their density and
476 structure form the foundation for physiological alterations in synaptic efficacy that
477 underlie learning and memory processes (41). We hypothesized that dendritic structure
478 and plasticity undergo alterations following SARS2-N501Y$_{MA30}$ infection. Fourteen days
479 after SARS2-N501Y$_{MA30}$ infection, brain slices containing the amygdala were
480 meticulously dissected, fixed, and subjected to Golgi staining to label the spines **(Fig.
481 4A)**. Neurons were randomly selected from within the basolateral amygdala, with a
482 focus on secondary branches located 50-100 μm away from the soma **(Fig. 4B, C)**.
483 Subsequently, spine morphology was manually visualized and analyzed **(Fig. 4D)**.
484
485 To characterize spine morphology, we categorized dendritic processes into two distinct
486 morphological classes: mature and immature spines (42). Mature spines, predominantly
487 exhibiting a "mushroom-like" morphology, exhibit more stable postsynaptic structures
488 enriched in α-amino-3-hydroxy-5-methyl-4-isoxazolepropionic acid receptors
489 (AMPARs) and are considered functional spines. Conversely, immature spines,
490 characterized by their thin, stubby, and filopodial features, represent unstable
491 postsynaptic structures with transitional properties. Immature dendritic spines are
492 believed to hold the potential for future synaptic plasticity, either maturing into functional
493 spines or disappearing from the dendrite (43). Spine categories were identified based

494 on parameters described in previous studies and Methods (35, 44).In the brains of mice
495 infected with SARS2-N501Y$_{MA30}$ (14 dpi), we found variations in spine subtypes, notably
496 an elevated proportion of mature spines compared to the mock infection group **(Fig.**
497 **4E)**. Combined with the gene expression profiles from **Fig. 3** and observations on
498 dendritic morphology, our findings indicate enhanced synaptic plasticity in amygdala
499 neurons fourteen days after SARS2-N501Y$_{MA30}$ infection.
500
501 **Spike protein increases microglia-dependent fEPSPs in amygdala slices**
502 Exposure to the SARS-CoV-2 spike protein has emerged as a topic of interest in
503 neurobiology, particularly regarding its impact on neuronal function. Previous research
504 has provided initial insights into how spike protein can influence neuronal morphology
505 and function (45-47). To further explore the mechanistic aspects of this phenomenon,
506 we focused on the amygdala, a region critically involved in emotional processing and
507 defensive behaviors. We perfused amygdala slices from mice with the recombinant
508 B1.351 variant spike protein (167 ng/ml), which has a high affinity to mouse ACE, and
509 monitored changes in fEPSPs for 2 hours **(Fig. 5A)**. We observed a significant increase
510 in fEPSPs following exposure to the B1.351 variant spike protein, indicating heightened
511 synaptic transmission and neuronal excitability **(Fig. 5B, C)**. Despite the fact that
512 whether SARS-CoV-2 spike protein increases or decreases neuronal activity is
513 controversial (45-48), this observation is noteworthy, as it suggests that the spike
514 protein, when directly interacting with neurons, has the potential to amplify their
515 responsiveness to incoming signals. This heightened neuronal response could, in turn,
516 render individuals more sensitive to various stimuli, potentially leading to alterations in
517 behaviors or physiological reactions. Interestingly, the administration of 50 μM
518 Resveratrol, a known inhibitor of microglial activation (49), effectively counteracted the
519 spike protein-induced enhancement of fEPSPs **(Fig. 5C, D)**. This finding suggests that
520 microglia, the intrinsic resident immune sentinels of the brain, may play a pivotal role in
521 mediating the effects of the spike protein on neuronal activity.
522
523 **Microglia activation after SARS-CoV-2 infection or exposure to spike protein**
524 Following the discovery in **Fig. 5**, we conducted further investigations into microglial

525 reactivity during SARS2-N501Y$_{MA30}$ infection. Through immunofluorescence staining for
526 Iba1, we documented a significant activation of microglia, evidenced by their
527 morphological shift from ramified to amoeboid shapes (50). This shift was notable at 4
528 days post-infection, by 14 days post-infection, microglia activity had not fully reverted to
529 the baseline quiescent state observed at 0 dpi, although it was substantially reduced
530 compared to 4 dpi, as illustrated in **Fig. 6A**. This finding provides further support for the
531 hypothesis that microglial activation may contribute to the observed alterations in
532 neuronal activities within the amygdala following SARS-CoV-2 infection.
533
534 Microglia, the brain's resident immune cells, are highly dynamic, engaging with neurons
535 and other brain cells upon activation. Their processes reach out to neighboring cells,
536 forming a complex network of interactions crucial for understanding the neuroimmune
537 impact of SARS-CoV-2 infection (51). To further elucidate the mechanism by which the
538 spike protein promoted microglia activation, we visualized microglia by
539 immunofluorescence staining for Iba1 in mouse amygdala slices. Our observations
540 confirmed the activation of microglia following SARS-CoV-2 B1.351 spike protein
541 perfusion **(Fig. 6B, C)**. Interestingly, the activation was attenuated by the purinoceptor
542 P2Y$_{12}$ (P2Y12R) antagonist ticlopidine **(Fig. 6C, D)**, indicating that the P2Y12R
543 signaling pathway mediates this response. P2Y$_{12}$, selectively expressed in microglia
544 (52), serves as the main adenosine triphosphate (ATP) receptor, initialing microglial
545 activation and mobilization in response to ATP, a potent neuronal chemoattractant
546 released from neurons (19, 53). Additionally, it is worth noting that SARS-CoV-2
547 infection has been shown to induce ATP release from host cells, including neural cells,
548 via specific channels (54, 55), a phenomenon we corroborated by detecting elevated
549 ATP levels in brain slices perfused with spike protein **(Fig. 6E, F)**.
550
551 **Brain Immune Inflammation and Anti-Viral Responses during Viral Infection**
552 Cytokines and chemokines serve as crucial indicators of anti-viral response and
553 immune inflammation. To delineate the immune responses within the brain during
554 SARS-CoV-2 infection, we conducted quantitative reverse-transcription PCR (RT-
555 qPCR) to profile cytokines and chemokines expression across various time points in the

556 brain **(Fig. 7)**. Contrary to expectations, the expression levels of interferon genes,
557 including IFN-β, γ, and λ, as well as the tumor necrosis factor gene, remained unaltered
558 in the infected brain tissues. However, it is noteworthy that transcripts encoding pro-
559 inflammatory cytokines, such as interleukin-1α (IL-1α), interleukin-6 (IL-6), interleukin-8
560 (IL8/CXCL1), and especially monocyte chemoattractant protein-1 (MCP1/CCL2),
561 exhibited significant upregulation at 2- or 4-days post-infection. These temporal
562 increases coincided with the presence of viral RNA in the brain. Importantly, it is worth
563 highlighting that the alterations observed in immune gene expression within the brain
564 were modest in comparison to those observed in the lungs and returned to baseline
565 levels after 6 days post-infection. This discovery underscores the presence of restrained
566 immune inflammation and anti-viral responses within the brain. The observed changes
567 in immune gene expression warrant further comprehensive investigations to unravel the
568 underlying mechanisms and identify potential targets for therapeutic intervention.
569

570 **DISCUSSION**

571 **Neurotropism of SARS-CoV-2 and Behavioral Alterations**

572 Our findings revealed the presence of SARS-CoV-2 in the CNS following intranasal
573 inoculation in a SARS2-N501Y$_{MA30}$ infection mouse model **(Fig.1)**. These results are
574 consistent with previous reports indicating that SARS-CoV-2 can invade the human
575 brain (5, 6), supporting the notion of neurotropism. SARS-CoV-2 probably enters the
576 central nervous system (CNS) through two potential pathways (56). The first involves
577 accessing the CNS via the neural-mucosal interface in the olfactory mucosa, enabling
578 the virus to spread from the periphery olfactory neurons into the neurons of the olfactory
579 bulb. The second pathway is through entry into the brain via blood circulation,
580 potentially breaching the blood-brain barrier (BBB). In this scenario, the integrity of the
581 BBB could be disrupted by inflammatory responses triggered by the infection.
582

583 Notably, the observed viral invasion of the CNS was accompanied by significant
584 alterations in anxiety- and depression-like behaviors, as evidenced by behavioral
585 assays **(Fig. 2)**. Anxiety and depression are prevalent neuropsychiatric disorders
586 associated with significant morbidity and mortality worldwide. The link between other

587 viral infections and mental health disturbances has been reported in previous studies,
588 with evidence of viral neuroinvasion contributing to behavioral changes (57, 58). Our
589 study provides valuable evidence supporting a direct association between SARS-CoV-2
590 neurotropism and anxiety- and depression-like behaviors. These findings underscore
591 the importance of considering the potential neuropsychiatric consequences of COVID-
592 19 and highlight the need for comprehensive mental health assessments and
593 interventions during and after the acute phase of infection.
594
595 **Microglial Activation, Neuroinflammation, and Neuronal Activity**
596 Microglia, as the primary immune cells of the CNS, play a critical role in maintaining
597 brain homeostasis and protecting against infections (59). Upon encountering pathogens
598 or damage signals, microglia undergo rapid activation, transforming from a surveillant to
599 an immune-responsive phenotype. In our study, we observed robust microglial
600 activation in brain regions where viral particles were detected, suggesting a potential
601 role for microglia in mediating SARS-CoV-2-induced neurobehavioral alterations. While
602 microglia itself may not be a direct target of SARS-CoV-2 infection (4, 60), the initial
603 invasion of SARS-CoV-2 in the neuron cells of the brain likely triggers their activation.
604 Microglial activation can lead to neuroinflammation, characterized by the release of pro-
605 inflammatory cytokines, chemokines, and reactive oxygen species (ROS). Chronic
606 neuroinflammation has been implicated in the pathogenesis of various neuropsychiatric
607 disorders, including anxiety and depression (61). Notably, our transcriptomic analysis of
608 SARS-CoV-2-infected brains revealed upregulation of inflammatory and cytokine-
609 related pathways, supporting the hypothesis of microglia-driven neuroinflammation as a
610 mechanism underlying behavioral changes. While our whole-brain qPCR and bulk RNA
611 seq revealed minimal changes in immune responses, it is conceivable that the immune
612 responses induced by SARS-CoV-2 are relatively subdued and localized to specific
613 brain regions. Therefore, the comprehensive assessment of whole-brain studies may
614 underestimate the extent of regional immune responses.
615
616 Purinergic receptor $P2Y_{12}$, a G protein-coupled receptor exclusively found in microglia
617 (52), played a pivotal role in the brain's responses to extracellular nucleotides like ATP

618 and ADP. Upon activation by ATP, microglia not only accumulate but also modulate
619 neuronal activity (16, 17), implicating ATP, known for its swift release from activated
620 neurons (62), as a swift mediator in the neuroimmune response to SARS2-N501Y$_{MA30}$
621 infection. This activation leads to the release of pro-inflammatory cytokines, which are
622 known to influence neuronal excitability and synaptic transmission (63), potentially
623 exacerbating anxiety- and depression-like behaviors (64). Indeed SARS-CoV-2 infection
624 has been shown to induce ATP release from brain cells, including neural cells, through
625 ATP-release channels (54, 55), reinforcing the link between infection and rapid ATP-
626 mediated microglia response. Clinical and laboratory studies support the idea that
627 elevated cytokines like IL-1β, IL-6, CCL2 and TNF-α associated with the development of
628 anxiety and depression-like behaviors in mice (65-68), underscoring the contribution of
629 neuroinflammation to the behavioral manifestations observed following SARS-CoV-2
630 infection. Our hypotheses detailing the interactions are visually summarized in **Fig. 8**,
631 providing a clear representation of the underlying mechanisms.
632
633 **Microglial Inhibition and Neuronal Activity Reversal**
634 To elucidate the specific role of microglia in mediating neuronal activity following SARS-
635 CoV-2 infection, we selectively inhibit microglia using a pharmacological approach.
636 Intriguingly, this inhibition markedly reduced the heightened neuronal activity induced by
637 viral spike protein. This observation indicates a direct involvement of microglia in the
638 development of abnormal neuronal activity in response to SARS-CoV-2 infection. The
639 observed neuronal activity rescue upon microglial inhibition aligns with previous studies
640 showing that microglial activation is a key driver of neuronal activity changes in various
641 CNS disorders (69). Understanding the interactions between microglia and neurons and
642 how SARS-CoV-2 infection influences these processes in the amygdala is crucial to
643 comprehending the neurological consequences of the virus. Such insights could offer
644 valuable information to guide potential interventions or treatments for neurological
645 manifestations observed in long COVID. Further research is needed to fully elucidate
646 the intricate mechanisms underlying microglial activation and its impact on neuronal
647 functions in response to SARS-CoV-2 infection in the brain.
648

649 **Inflammatory Pathways and Therapeutic Interventions**

650 Our hypothesis suggests that microglia-driven neuroinflammation contributes to the
651 behavioral changes seen in long COVID-19. This highlights the therapeutic potential of
652 targeting neuroinflammatory pathways to ameliorate anxiety- and depression-like
653 symptoms associated with the disease. The transcriptomic analysis of brains affected
654 by the virus has identified upregulated inflammatory pathways, indicating potential
655 targets for therapeutic interventions. Anti-inflammatory agents and immunomodulatory
656 drugs that selectively dampen microglial activation may offer a promising approach for
657 treating the neuropsychiatric consequences of SARS-CoV-2 infection. However, further
658 research is needed to identify specific inflammatory mediators and downstream
659 signaling pathways responsible for the observed behavioral changes.

660

661 **Limitations and Future Directions**

662 While our study provides valuable insights into the link between SARS-CoV-2
663 neurotropism, microglial activation, neuronal activity, and anxiety- and depression-like
664 behaviors, several limitations should be acknowledged.

665

666 First, in our pursuit to unravel the etiology of neurological disorders post-COVID-19, we
667 identified behavioral phenotypes emerging within weeks post-infection. The onset of
668 neurological symptoms post-COIVD-19 can vary greatly among individuals, manifesting
669 during the acute phase, post-recovery, or even several months later. The persistence of
670 PASC symptoms in humans can range from weeks to several months, and in some
671 cases, may extend even further. We acknowledge the differences in lifespan and
672 sensitivity to SARS-CoV-2 between our murine model and human subjects. We chose
673 the 14-day time point for behavioral testing as viral infections were observed to have
674 cleared, and the conditions of infected mice had fully recovered. This rapid recovery in
675 the mouse model confers a significant advantage for our mechanistic studies,
676 eliminating the need for a year-long wait. To improve upon our research model and
677 better mimic human conditions, we plan to extend the testing duration by incorporating
678 additional time points up to at least one year in future studies. Furthermore, the
679 prolonged effects of SARS-CoV-2 on mental health necessitate further investigation.

680 Second, we used a murine model, and findings in rodents may not fully translate to
681 human conditions. Future research should explore the temporal dynamics of microglial
682 activation and neuroinflammation throughout different stages of SARS-CoV-2 infection.
683
684 Third, we identified that brain infection in mice developed mild respiratory diseases. We
685 did not further evaluate the case of asymptomatic infection because a clinical study
686 suggested that the risk of developing long-term symptoms in asymptomatic SARS-CoV-
687 2 infected persons was significantly lower than those in symptomatic SARS-CoV-2
688 infection cases (70).
689
690 Fourth, we utilized a mouse-adapted SARS-CoV-2 strain that shares some key spike
691 mutations with the Beta variant. However, the specific potential, impact, and severity of
692 neuroinvasion resulting from different SARS-CoV-2 variants, such as the Omicron
693 variant, and the potential effects of breakthrough infections in vaccinated individuals,
694 remain areas that require further investigation to provide a comprehensive
695 understanding.
696
697 Fifth, we did not systematically investigate the potential impact of elevated cytokines
698 and chemokines induced by respiratory COVID-19 on microglial activation and their
699 potential effects on impairing CNS neuron function. It is well-established that exposure
700 to chemotherapy drugs, brain radiation, or systemic inflammation can lead to persistent
701 activation of certain microglia (1, 71-74). Interestingly, a recent study of SARS-CoV-2
702 infection in AAV-hACE2 sensitized mice or H1N1 influenza infection in mice revealed
703 that mild respiratory disease-activated white-matter-selective microglia, leading to
704 oligodendrocyte loss, impaired neurogenesis, and elevated CCL11 levels (75). These
705 findings highlight the potential impact of systemic inflammation on microglia activation
706 and brain function. Longitudinal studies in human cohorts are necessary to establish
707 causality between viral neurotropism, microglial activation, and neuropsychiatric
708 outcomes. Moreover, investigating potential sex-dependent differences in behavioral
709 responses and microglial activation can provide a more comprehensive understanding
710 of COVID-19-associated neuropsychiatric sequelae. Addressing these limitations

711 through further research is essential to advance our understanding of the complex
712 neurological effects of SARS-CoV-2 infection and its variants. By exploring these areas
713 further, we can gain valuable insights to develop more effective interventions and
714 treatment strategies for individuals affected by COVID-19 and its neurological
715 consequences. The evaluation of the consequences of $N501Y_{MA30}$ infection on the CNS
716 has provided valuable insights, positioning this mouse-adapted strain as an auspicious
717 model for studying the neurological manifestations of PASC. Continuation of research
718 utilizing this mouse model, alongside other relevant models, is pivotal in advancing our
719 understanding of the neurological effects of SARS-CoV-2 and facilitating the
720 development of effective interventions for PASC.
721
722 Finally, we utilized bulk RNA-sequencing to analyze gene changes following viral
723 infection. However, this approach may not fully capture gene changes in specific cell
724 types, such as microglia, which could potentially confound the observed neuron-
725 microglia interactions. To precisely elucidate the immune response and subsequent
726 changes in neuronal activity genes, future studies should consider supplementing with
727 single-cell RNA-seq focusing on specific brain regions.
728
729 **Conclusion**
730 Our study demonstrates that SARS-CoV-2 neurotropism induces anxiety- and
731 depression-like behaviors through the activation of microglia and subsequent
732 neuroinflammation. These findings underscore the importance of considering mental
733 health disturbances in COVID-19 patients and emphasize the need for integrated
734 approaches to address both the physical and mental health aspects of the pandemic.
735 Targeting microglial activation and neuroinflammatory pathways may offer promising
736 therapeutic avenues to mitigate the neurobehavioral consequences of SARS-CoV-2
737 infection. Further investigations in human cohorts are warranted to validate and extend
738 our preclinical findings for potential translational applications.
739
740 **AUTHOR CONTRIBUTIONS**

741 J.D. and K.L. conceived the project. J.D., K.L., and Q.G. designed the experiments.
742 Q.G. and J.D. performed the patch-clamp and immunostaining experiments and data
743 analysis. S.Z. and K.L. performed the behavior and molecular experiments and data
744 analysis. K.L., J.D., and Q.G. wrote the manuscript. All authors reviewed and edited the
745 manuscript.
746

747 **ACKNOWLEDGMENTS**

748 J.D. is supported by the National Institutes of Mental Health (1R01MH113986), the
749 Cystic Fibrosis Foundation (002544I221), and the University of Tennessee Health
750 Science Center start-up fund. K.L. is supported by the Cystic Fibrosis Foundation and
751 the Cleveland Clinic Florida Research and Innovation Center start-up fund.
752

753 **CONFLICT-OF-INTEREST**

754 The authors have declared that no conflict of interest exists.
755

756 **REFERENCES**

757 1. A. C. Geraghty *et al.*, Loss of Adaptive Myelination Contributes to Methotrexate
758 Chemotherapy-Related Cognitive Impairment. *Neuron* **103**, 250-265 e258
759 (2019).
760 2. Z. A. Sherif *et al.*, Pathogenic mechanisms of post-acute sequelae of SARS-
761 CoV-2 infection (PASC). *Elife* **12** (2023).
762 3. B. Bowe, Y. Xie, Z. Al-Aly, Postacute sequelae of COVID-19 at 2 years. *Nat Med*
763 **29**, 2347-2357 (2023).
764 4. M. G. Andrews *et al.*, Tropism of SARS-CoV-2 for human cortical astrocytes.
765 *Proc Natl Acad Sci U S A* **119**, e2122236119 (2022).
766 5. E. Song *et al.*, Neuroinvasion of SARS-CoV-2 in human and mouse brain. *J Exp*
767 *Med* **218** (2021).
768 6. S. R. Stein *et al.*, SARS-CoV-2 infection and persistence in the human body and
769 brain at autopsy. *Nature* **612**, 758-763 (2022).
770 7. M. F. DosSantos *et al.*, Neuromechanisms of SARS-CoV-2: A Review. *Front*
771 *Neuroanat* **14**, 37 (2020).
772 8. A. Pepe, S. Pietropaoli, M. Vos, G. Barba-Spaeth, C. Zurzolo, Tunneling
773 nanotubes provide a route for SARS-CoV-2 spreading. *Sci Adv* **8**, eabo0171
774 (2022).
775 9. M. G. Savelieff, E. L. Feldman, A. M. Stino, Neurological sequela and disruption
776 of neuron-glia homeostasis in SARS-CoV-2 infection. *Neurobiol Dis* **168**, 105715
777 (2022).
778 10. D. Davalos *et al.*, ATP mediates rapid microglial response to local brain injury in
779 vivo. *Nat Neurosci* **8**, 752-758 (2005).

11. A. Nimmerjahn, F. Kirchhoff, F. Helmchen, Resting microglial cells are highly dynamic surveillants of brain parenchyma in vivo. *Science* **308**, 1314-1318 (2005).
12. R. M. Ransohoff, V. H. Perry, Microglial physiology: unique stimuli, specialized responses. *Annu Rev Immunol* **27**, 119-145 (2009).
13. H. Wake, A. J. Moorhouse, S. Jinno, S. Kohsaka, J. Nabekura, Resting microglia directly monitor the functional state of synapses in vivo and determine the fate of ischemic terminals. *J Neurosci* **29**, 3974-3980 (2009).
14. M. E. Tremblay, R. L. Lowery, A. K. Majewska, Microglial interactions with synapses are modulated by visual experience. *PLoS Biol* **8**, e1000527 (2010).
15. K. M. Lucin, T. Wyss-Coray, Immune activation in brain aging and neurodegeneration: too much or too little? *Neuron* **64**, 110-122 (2009).
16. Q. Li, B. A. Barres, Microglia and macrophages in brain homeostasis and disease. *Nat Rev Immunol* **18**, 225-242 (2018).
17. D. P. Schafer, E. K. Lehrman, B. Stevens, The "quad-partite" synapse: microglia-synapse interactions in the developing and mature CNS. *Glia* **61**, 24-36 (2013).
18. D. J. Stein, M. F. Vasconcelos, L. Albrechet-Souza, K. M. M. Cereser, R. M. M. de Almeida, Microglial Over-Activation by Social Defeat Stress Contributes to Anxiety- and Depressive-Like Behaviors. *Front Behav Neurosci* **11**, 207 (2017).
19. U. B. Eyo *et al.*, Neuronal hyperactivity recruits microglial processes via neuronal NMDA receptors and microglial P2Y12 receptors after status epilepticus. *J Neurosci* **34**, 10528-10540 (2014).
20. A. M. Fontainhas *et al.*, Microglial morphology and dynamic behavior is regulated by ionotropic glutamatergic and GABAergic neurotransmission. *PLoS One* **6**, e15973 (2011).
21. Y. Li, X. F. Du, C. S. Liu, Z. L. Wen, J. L. Du, Reciprocal regulation between resting microglial dynamics and neuronal activity in vivo. *Dev Cell* **23**, 1189-1202 (2012).
22. J. Damas *et al.*, Broad host range of SARS-CoV-2 predicted by comparative and structural analysis of ACE2 in vertebrates. *Proc Natl Acad Sci U S A* **117**, 22311-22322 (2020).
23. M. A. A. Mahdy, W. Younis, Z. Ewaida, An Overview of SARS-CoV-2 and Animal Infection. *Front Vet Sci* **7**, 596391 (2020).
24. D. V. Glazkova *et al.*, Generation of SARS-CoV-2 Mouse Model by Transient Expression of the Human ACE2 Gene Mediated by Intranasal Administration of AAV-hACE2. *Mol Biol* **56**, 705-712 (2022).
25. J. Sun *et al.*, Generation of a Broadly Useful Model for COVID-19 Pathogenesis, Vaccination, and Treatment. *Cell* **182**, 734-743 e735 (2020).
26. J. Zheng *et al.*, COVID-19 treatments and pathogenesis including anosmia in K18-hACE2 mice. *Nature* **589**, 603-607 (2021).
27. L. R. Wong *et al.*, Eicosanoid signalling blockade protects middle-aged mice from severe COVID-19. *Nature* **605**, 146-151 (2022).
28. P. H. Janak, K. M. Tye, From circuits to behaviour in the amygdala. *Nature* **517**, 284-292 (2015).

824 29. L. R. Wong *et al.*, Sensitization of Non-permissive Laboratory Mice to SARS-
825 CoV-2 with a Replication-Deficient Adenovirus Expressing Human ACE2. *STAR*
826 *Protoc* **1**, 100169 (2020).
827 30. A. A. Walf, C. A. Frye, The use of the elevated plus maze as an assay of anxiety-
828 related behavior in rodents. *Nat Protoc* **2**, 322-328 (2007).
829 31. J. Du *et al.*, Transient acidosis while retrieving a fear-related memory enhances
830 its lability. *Elife* **6** (2017).
831 32. G. Matute-Bello *et al.*, An official American Thoracic Society workshop report:
832 features and measurements of experimental acute lung injury in animals. *Am J*
833 *Respir Cell Mol Biol* **44**, 725-738 (2011).
834 33. F. Levet, J. Tonnesen, U. V. Nagerl, J. B. Sibarita, SpineJ: A software tool for
835 quantitative analysis of nanoscale spine morphology. *Methods* **174**, 49-55
836 (2020).
837 34. C. J. Kreple *et al.*, Acid-sensing ion channels contribute to synaptic transmission
838 and inhibit cocaine-evoked plasticity. *Nat Neurosci* **17**, 1083-1091 (2014).
839 35. W. J. Wright *et al.*, Silent synapses dictate cocaine memory destabilization and
840 reconsolidation. *Nat Neurosci* **23**, 32-46 (2020).
841 36. H. Shuai *et al.*, Emerging SARS-CoV-2 variants expand species tropism to
842 murines. *EBioMedicine* **73**, 103643 (2021).
843 37. F. Rigoli, M. Ewbank, T. Dalgleish, A. Calder, Threat visibility modulates the
844 defensive brain circuit underlying fear and anxiety. *Neurosci Lett* **612**, 7-13
845 (2016).
846 38. K. M. Woolfrey, D. P. Srivastava, Control of Dendritic Spine Morphological and
847 Functional Plasticity by Small GTPases. *Neural Plast* **2016**, 3025948 (2016).
848 39. G. Yang, F. Pan, W. B. Gan, Stably maintained dendritic spines are associated
849 with lifelong memories. *Nature* **462**, 920-924 (2009).
850 40. J. N. Bourne, K. M. Harris, Balancing structure and function at hippocampal
851 dendritic spines. *Annu Rev Neurosci* **31**, 47-67 (2008).
852 41. C. H. Bailey, E. R. Kandel, K. M. Harris, Structural Components of Synaptic
853 Plasticity and Memory Consolidation. *Cold Spring Harb Perspect Biol* **7**, a021758
854 (2015).
855 42. A. Peters, I. R. Kaiserman-Abramof, The small pyramidal neuron of the rat
856 cerebral cortex. The perikaryon, dendrites and spines. *Am J Anat* **127**, 321-355
857 (1970).
858 43. K. P. Berry, E. Nedivi, Spine Dynamics: Are They All the Same? *Neuron* **96**, 43-
859 55 (2017).
860 44. E. E. Koffman *et al.*, Acid-sensing ion channel 1a regulates the specificity of
861 reconsolidation of conditioned threat responses. *JCI Insight*
862 10.1172/jci.insight.155341 (2022).
863 45. J. Oh *et al.*, SARS-CoV-2 spike protein induces cognitive deficit and anxiety-like
864 behavior in mouse via non-cell autonomous hippocampal neuronal death. *Sci*
865 *Rep* **12**, 5496 (2022).
866 46. C.-Y. Chen, Y.-C. Chou, Y.-P. Hsueh, SARS-CoV-2 D614 and G614 spike
867 variants impair neuronal synapses and exhibit differential fusion ability. *BioRxiv*
868 10.1101/2020.12.03.409763 (2020).

869 47. M. G. Frank *et al.*, SARS-CoV-2 spike S1 subunit induces neuroinflammatory,
870 microglial and behavioral sickness responses: Evidence of PAMP-like properties.
871 *Brain Behav Immun* **100**, 267-277 (2022).
872 48. G. Datta *et al.*, SARS-CoV-2 S1 Protein Induces Endolysosome Dysfunction and
873 Neuritic Dystrophy. *Front Cell Neurosci* **15**, 777738 (2021).
874 49. S. Zhang *et al.*, Resveratrol Attenuates Microglial Activation via SIRT1-SOCS1
875 Pathway. *Evid Based Complement Alternat Med* **2017**, 8791832 (2017).
876 50. A. Vidal-Itriago *et al.*, Microglia morphophysiological diversity and its implications
877 for the CNS. *Front Immunol* **13**, 997786 (2022).
878 51. M. Colonna, O. Butovsky, Microglia Function in the Central Nervous System
879 During Health and Neurodegeneration. *Annu Rev Immunol* **35**, 441-468 (2017).
880 52. S.-S. Lin, Y. Tang, P. Illes, A. Verkhratsky, The Safeguarding Microglia: Central
881 Role for P2Y12 Receptors. *Frontiers in Pharmacology* **11** (2021).
882 53. L. J. Wu, K. I. Vadakkan, M. Zhuo, ATP-induced chemotaxis of microglial
883 processes requires P2Y receptor-activated initiation of outward potassium
884 currents. *Glia* **55**, 810-821 (2007).
885 54. R. Luu *et al.*, Pannexin-1 channel opening is critical for COVID-19 pathogenesis.
886 *iScience* **24**, 103478 (2021).
887 55. D. E. Ribeiro *et al.*, Hyperactivation of P2X7 receptors as a culprit of COVID-19
888 neuropathology. *Mol Psychiatry* **26**, 1044-1059 (2021).
889 56. S. M. Burks, H. Rosas-Hernandez, M. Alejandro Ramirez-Lee, E. Cuevas, J. C.
890 Talpos, Can SARS-CoV-2 infect the central nervous system via the olfactory bulb
891 or the blood-brain barrier? *Brain Behav Immun* **95**, 7-14 (2021).
892 57. K. Tomonaga, Virus-induced neurobehavioral disorders: mechanisms and
893 implications. *Trends Mol Med* **10**, 71-77 (2004).
894 58. I. Kotsiri *et al.*, Viral Infections and Schizophrenia: A Comprehensive Review.
895 *Viruses* **15** (2023).
896 59. M. E. Tremblay, C. Madore, M. Bordeleau, L. Tian, A. Verkhratsky,
897 Neuropathobiology of COVID-19: The Role for Glia. *Front Cell Neurosci* **14**,
898 592214 (2020).
899 60. D. Beckman *et al.*, SARS-CoV-2 infects neurons and induces neuroinflammation
900 in a non-human primate model of COVID-19. *Cell Rep* **41**, 111573 (2022).
901 61. S. J. Rhie, E. Y. Jung, I. Shim, The role of neuroinflammation on pathogenesis of
902 affective disorders. *J Exerc Rehabil* **16**, 2-9 (2020).
903 62. R. D. Fields, Nonsynaptic and nonvesicular ATP release from neurons and
904 relevance to neuron-glia signaling. *Semin Cell Dev Biol* **22**, 214-219 (2011).
905 63. M. Schafers, L. Sorkin, Effect of cytokines on neuronal excitability. *Neurosci Lett*
906 **437**, 188-193 (2008).
907 64. N. Vogelzangs, P. de Jonge, J. H. Smit, S. Bahn, B. W. Penninx, Cytokine
908 production capacity in depression and anxiety. *Transl Psychiatry* **6**, e825 (2016).
909 65. S. Rossi *et al.*, Interleukin-1beta causes anxiety by interacting with the
910 endocannabinoid system. *J Neurosci* **32**, 13896-13905 (2012).
911 66. R. K. Farooq, K. Asghar, S. Kanwal, A. Zulqernain, Role of inflammatory
912 cytokines in depression: Focus on interleukin-1beta. *Biomed Rep* **6**, 15-20
913 (2017).

67. M. A. Alshammari *et al.*, Systemic TNF-alpha blockade attenuates anxiety and depressive-like behaviors in db/db mice through downregulation of inflammatory signaling in peripheral immune cells. *Saudi Pharm J* **28**, 621-629 (2020).
68. J. Wojcieszak, K. Kuczynska, J. B. Zawilska, Role of Chemokines in the Development and Progression of Alzheimer's Disease. *J Mol Neurosci* **72**, 1929-1951 (2022).
69. J. Qin, Z. Ma, X. Chen, S. Shu, Microglia activation in central nervous system disorders: A review of recent mechanistic investigations and development efforts. *Front Neurol* **14**, 1103416 (2023).
70. Y. Ma *et al.*, Long-Term Consequences of Asymptomatic SARS-CoV-2 Infection: A Systematic Review and Meta-Analysis. *Int J Environ Res Public Health* **20** (2023).
71. E. M. Gibson *et al.*, Methotrexate Chemotherapy Induces Persistent Tri-glial Dysregulation that Underlies Chemotherapy-Related Cognitive Impairment. *Cell* **176**, 43-55 e13 (2019).
72. M. L. Monje, S. Mizumatsu, J. R. Fike, T. D. Palmer, Irradiation induces neural precursor-cell dysfunction. *Nat Med* **8**, 955-962 (2002).
73. M. L. Monje, H. Toda, T. D. Palmer, Inflammatory blockade restores adult hippocampal neurogenesis. *Science* **302**, 1760-1765 (2003).
74. M. L. Monje *et al.*, Impaired human hippocampal neurogenesis after treatment for central nervous system malignancies. *Ann Neurol* **62**, 515-520 (2007).
75. A. Fernandez-Castaneda *et al.*, Mild respiratory COVID can cause multi-lineage neural cell and myelin dysregulation. *Cell* **185**, 2452-2468 e2416 (2022).

Figure. 1

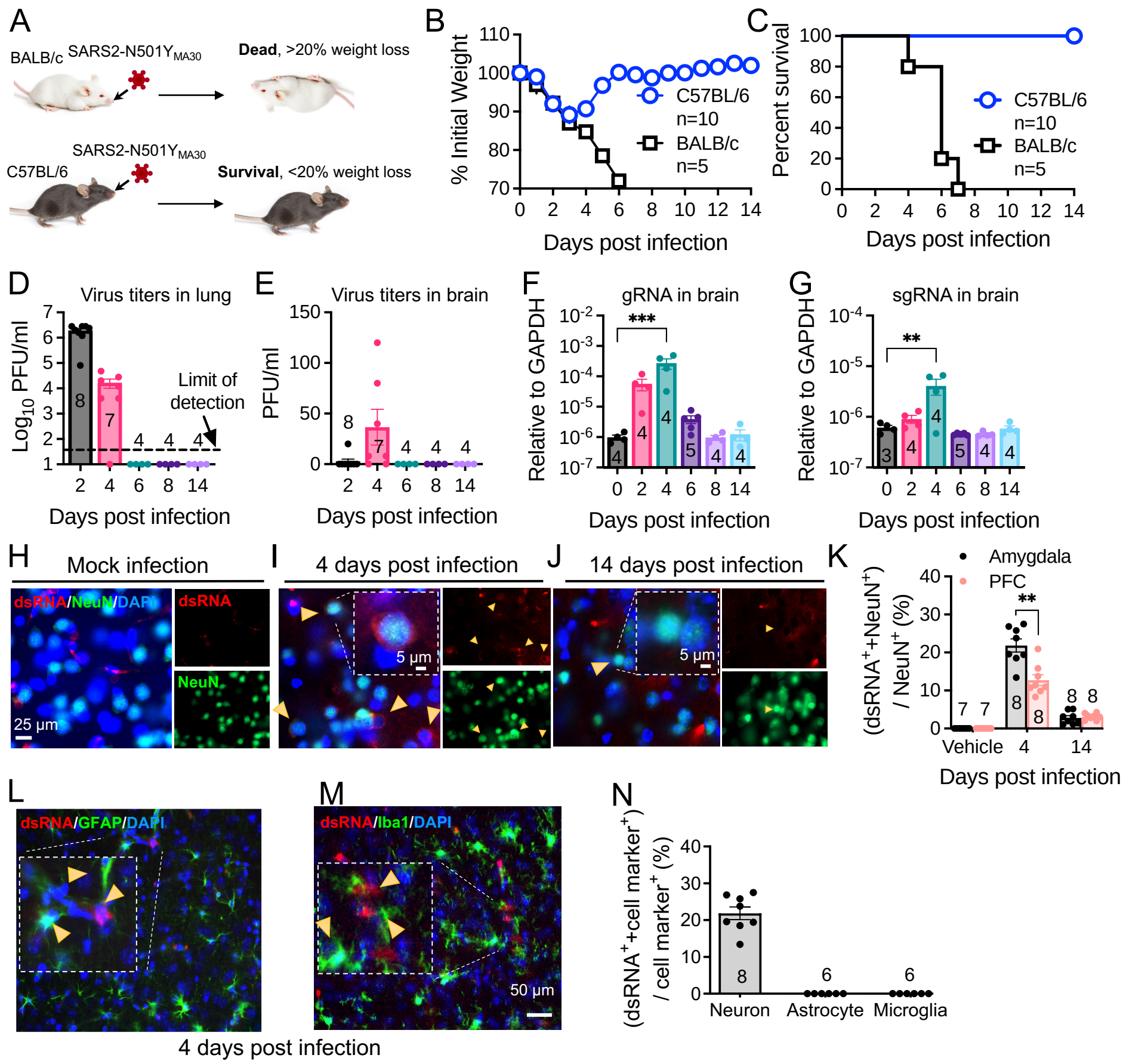

Figure. 1. Outcomes of Intranasal Infection with SARS2-N501Y$_{MA30}$. (A) Schematic depicting the outcomes of infection in young BALB/c and C57BL/6 mice following administration of 10^4 PFU of SARS2-N501Y$_{MA30}$. **(B-C)** Daily monitoring of body weight (B) and survival (C) in young BALB/c and C57BL/6 mice post-infection. **(D-E)** Virus titers in the lungs (D) and brains (E) of C57BL/6 mice infected with SARS2-N501Y$_{MA30}$ at the indicated days post-infection. **(F-G)** Viral genomic RNA (gRNA) (F) and subgenomic RNA (sgRNA) (G) levels in brain tissues from SARS2-N501Y$_{MA30}$ infected C57BL/6 mice. The levels of viral gRNA and sgRNA were normalized to GAPDH and presented as 2^-ΔCT (n = 4 or 5 mice per group). CT values for viral genomic RNA (gRNA) or subgenomic RNA (sgRNA) from mock-infected tissues were consistently greater than 35. Statistical significance: ***p = 0.001, **p = 0.0017, determined by ordinary one-way ANOVA. **(H-J)** Immunofluorescence staining targeting dsRNA (red), neuronal nuclear protein (NeuN, green), and nuclei (DAPI, blue) in amygdala brain slices collected from mice infected with SARS2-N501Y$_{MA30}$ infection at 4 or 14 days post (I-J), compared to mock infection (H). Arrows indicate dsRNA and NeuN-positive neurons. Inserts show enlarged single-cell images. **(K)** Percentage of dsRNA-positive cells (dsRNA$^+$) in slices from the amygdala and the prefrontal cortex (PFC). The peak of dsRNA$^+$ cells is observed at 4 dpi. Statistical significance: **p = 0.0012, determined by a two-tailed unpaired Student's t-test. **(L-M)** Immunofluorescence targeting dsRNA (red), astrocyte (glial fibrillary acidic protein, GFAP, green) or microglia (Ionized calcium-binding adaptor molecule 1, Iba1, green), and nuclei (DAPI, blue) in amygdala slices from infected mice. **(N)** Comparison of dsRNA$^+$ cells with NeuN$^+$, GFAP$^+$, and Iba1$^+$ at 4 dpi. . Data are presented as mean ± SEM.

Figure. 2

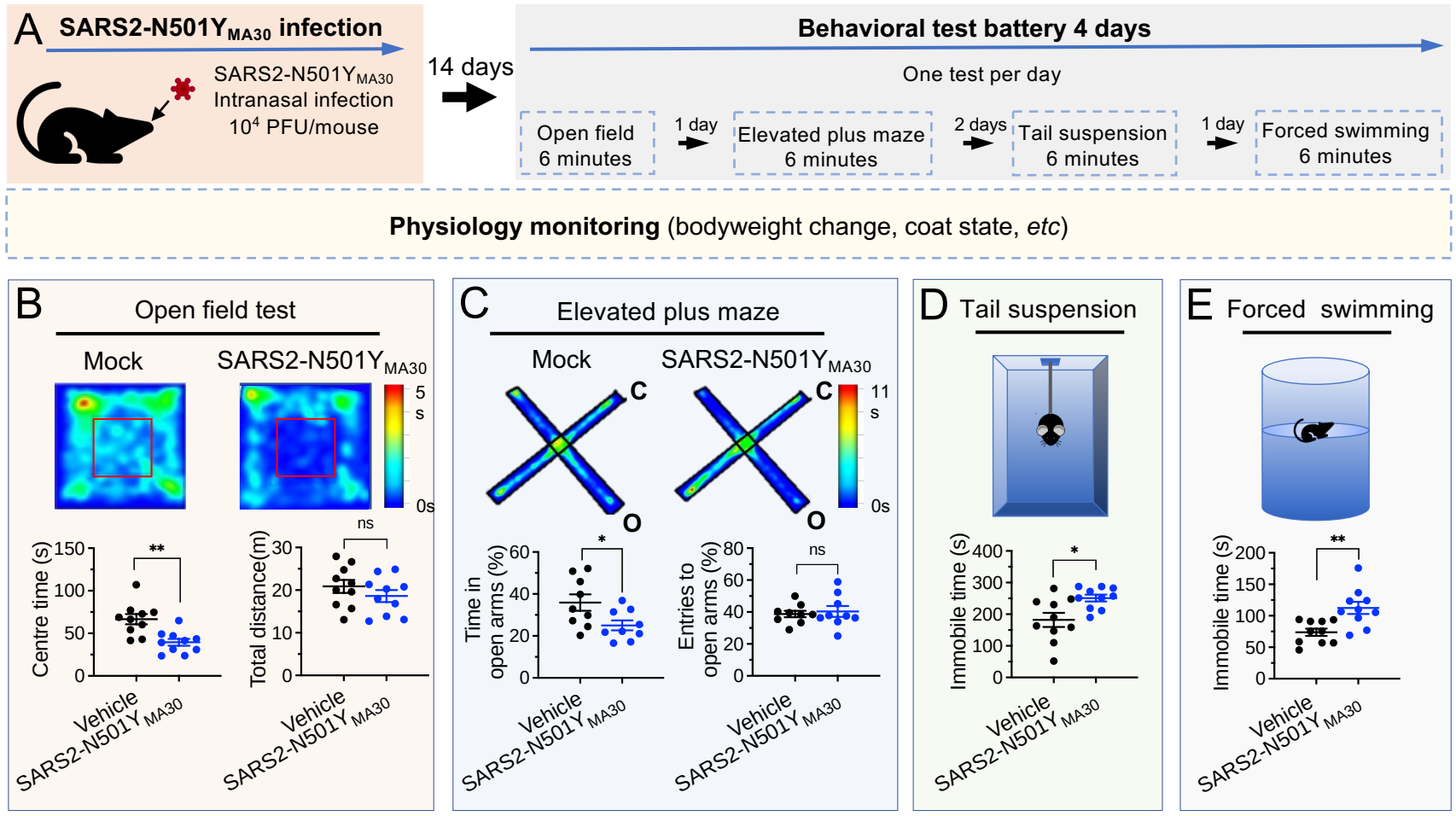

Figure. 2. Induction of anxiety- and depression-like Behaviors in Mice Following SARS2-N501Y$_{MA30}$ infection. (A) Experimental design and timeline illustrating the administration of SARS2-N501Y$_{MA30}$ and the behavioral test battery. **(B)** Open field test. Upper: Representative heat map tracking of activity in the mock and SARS2-N501Y$_{MA30}$ infected mice. Lower: Results depicting the total travel distance and time spent in the center area. Statistical significance: **p = 0.0014 (total travel distance); ns, non-significant, p = 0.2927 (center area). **(C)** Elevated plus maze test. Upper: Representative heat map tracking of activity in mock and SARS2-N501Y$_{MA30}$ infected mice in closed arms (C) and open arms (O). Lower: Results indicating the time spent in open arms and the number of entries into open arms. Statistical significance: *p = 0.0299 (time spent in open arms); ns, non-significant, p = 0.6897 (number of entries). **(D-E)** Schematics of the tail suspension (D) and forced swimming (E) tests and results showing immobile time. Statistical significance: *p = 0.0118 (tail suspension test); **p = 0.0029 (forced swimming test). All statistical analyses were performed using a two-tailed unpaired Student's t-test. The analysis includes data from 10 mice in each group. Data are presented as mean ± SEM.

Figure. 3

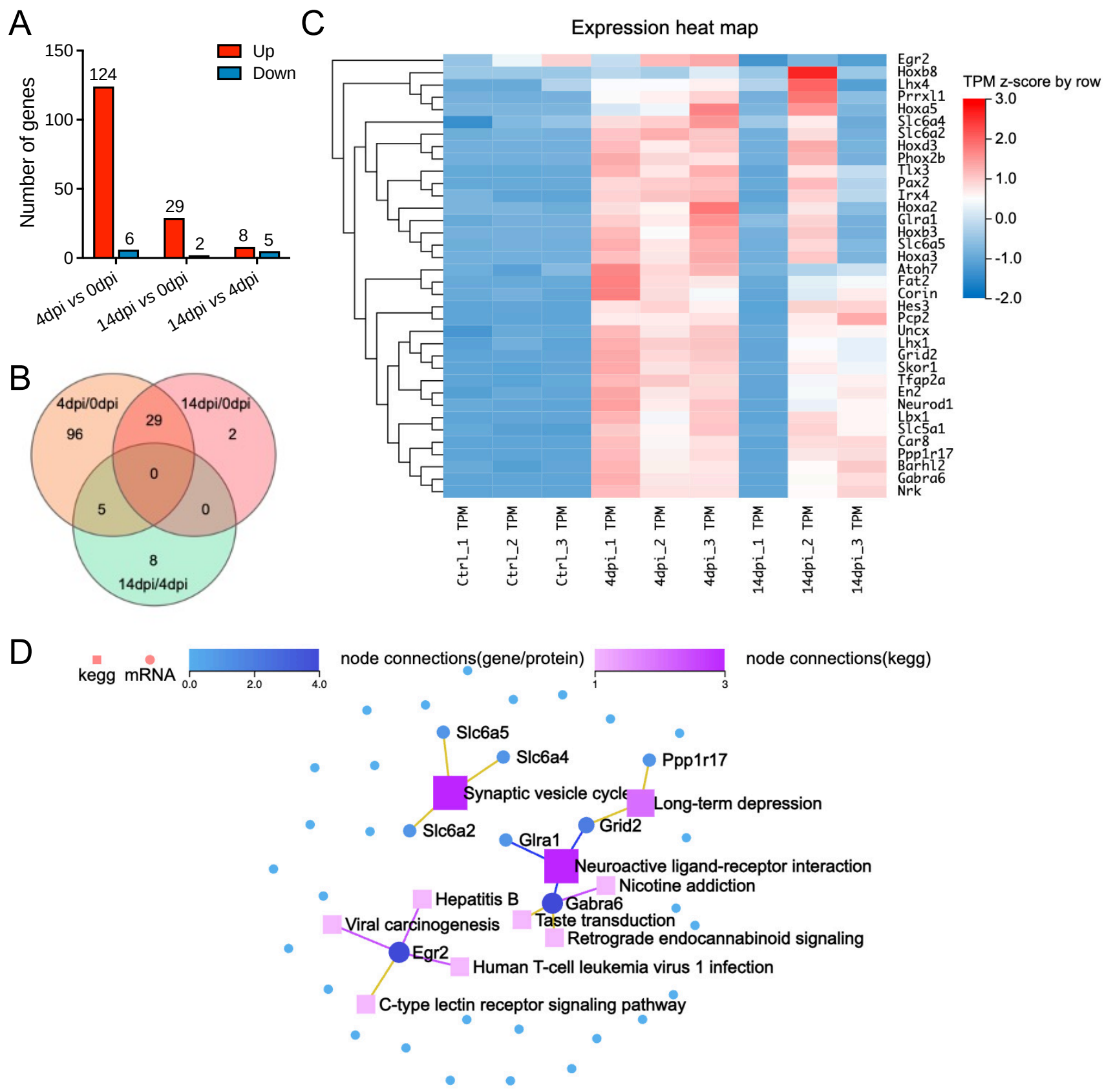

Figure. 3. RNA sequencing reveals distinct alterations in the brains of SARS2-N501Y$_{MA30}$ Infected Mice. (A) Histogram represents the corresponding numbers of differentially expressed genes (DEGs) between groups. (|log2fold| ≥ 1.5, Q value ≤ 0.05) **(B)** Venn diagram illustrating the differential gene expression analysis between groups of gene sets. The intersections show shared gene expression patterns, while non-overlapping regions indicate uniquely expressed genes. The numbers within each section denote the count of genes. **(C)** Heatmap displaying hierarchical clustering of 36 selected genes associated with neuron functions. **(D)** KEGG Network analysis of key driver genes and enriched KEGG pathways among the 36 selected genes. Dots symbolize genes, squares represent KEGG pathways, and lines connecting genes to squares signify gene enrichment within the respective pathway.

Figure. 4

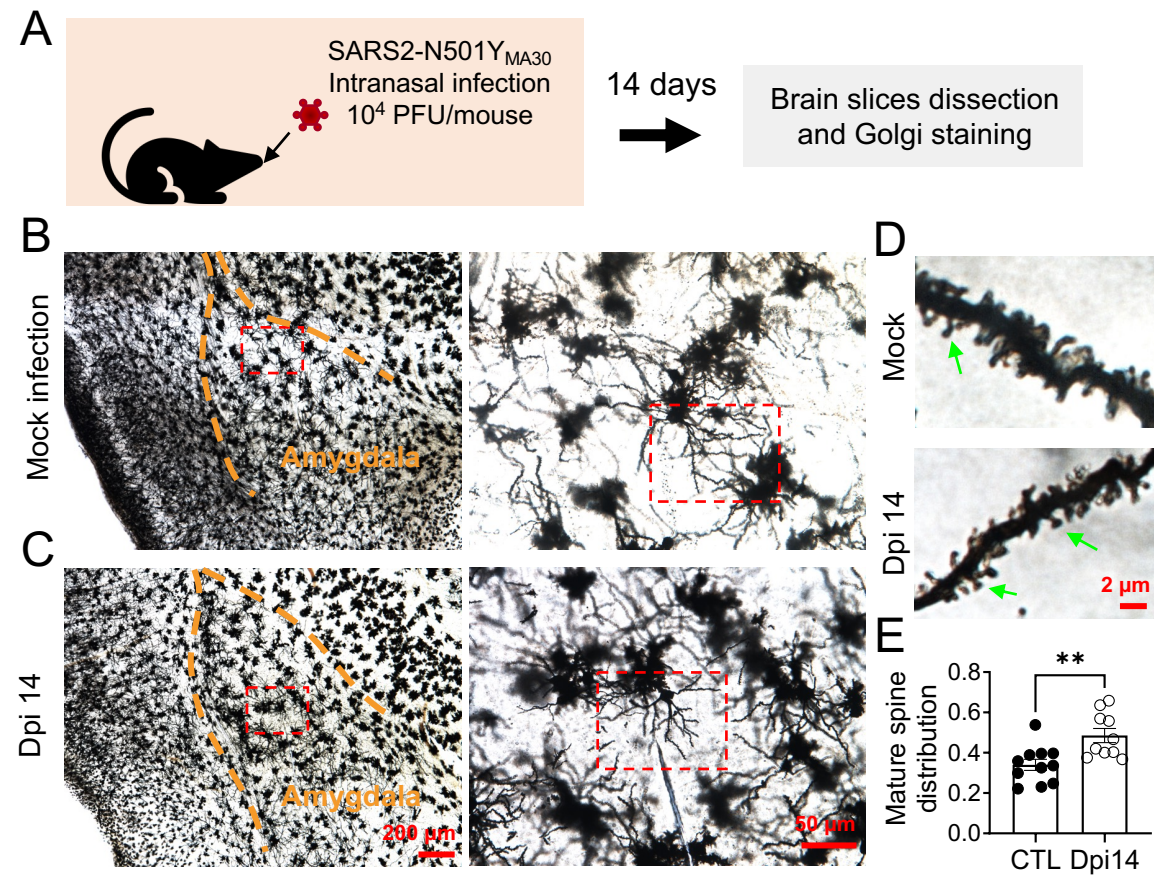

Figure. 4. Golgi-Cox Staining of Neurons in the Amygdala of SARS2-N501Y$_{MA30}$ Infected Mice. (A) Experimental design and timeline depicting the administration of SARS2-N501Y$_{MA30}$, dissection of brain slices, and Golgi staining process. **(B-C)** Left: Representative Golgi-Cox staining images of amygdala slices from mock-infected (B) and mice infected with SARS2-N501Y$_{MA30}$ at 14 days post-infection (dpi) (C). Scale bar = 200 μm. Right: Enlarged images from the red boxes in the left images for each respective group. Scale bar = 50 μm. **(D)** Representative dendrite images from the red boxes in (B) and (C). Scale bar = 2 μm. Green arrows point out the mushroom spines. **(E)** Comparison of the percentage of mature spines in the mock and SARS2-N501Y$_{MA30}$ infection groups. Statistical significance: **p = 0.0038. The analysis includes data from 11 neurons sourced from 4 mice in each group. Statistical analysis was performed using a two-tailed unpaired Student's t-test. Data are presented as mean ± SEM.

Figure. 5

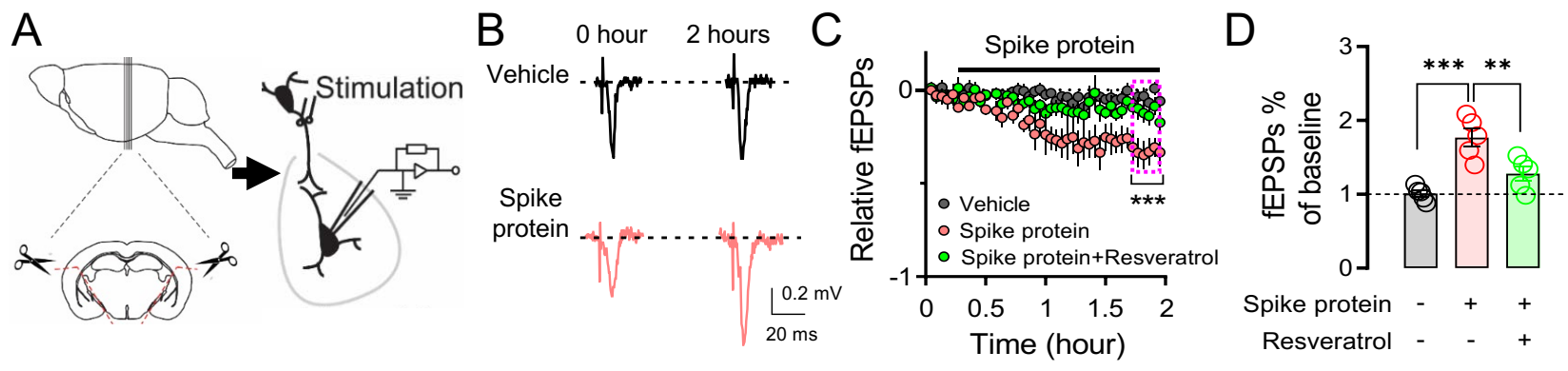

Figure. 5. Enhancement of Microglia-Dependent fEPSPs in the Amygdala by SARS-CoV-2 Variant B.1.351 Spike Protein. (A) Schematic representation of field excitatory postsynaptic potential (fEPSP) recordings in the Amygadala brain slices. **(B)** Representative fEPSP traces were recorded at the beginning (0 hours) and the end of the 2-hour recordings, during perfusion with either vehicle or spike protein (S1+S2, B.1.351, β variant, BPS Bioscience #510333, 167 ng/ml). **(C)** Average fEPSP data. The spike protein was applied to the slice (167 ng/ml) at the indicated time point (red trace). In the vehicle group, a mock aqueous buffer solution without the spike protein was used (gray trace). The enhancement of fEPSPs by the spike protein was attenuated by pre-treating brain slices with 50 μM Resveratrol (green trace). **(D)** Summarized amplitudes of the last five fEPSPs as shown in (C). Statistical significance: ***p = 0.0003, **p = 0.0082, determined by one-way ANOVA with Tukey's post hoc multiple comparisons. The analysis includes data from 5 slices in each group. Data are presented as mean ± SEM.

Figure. 6

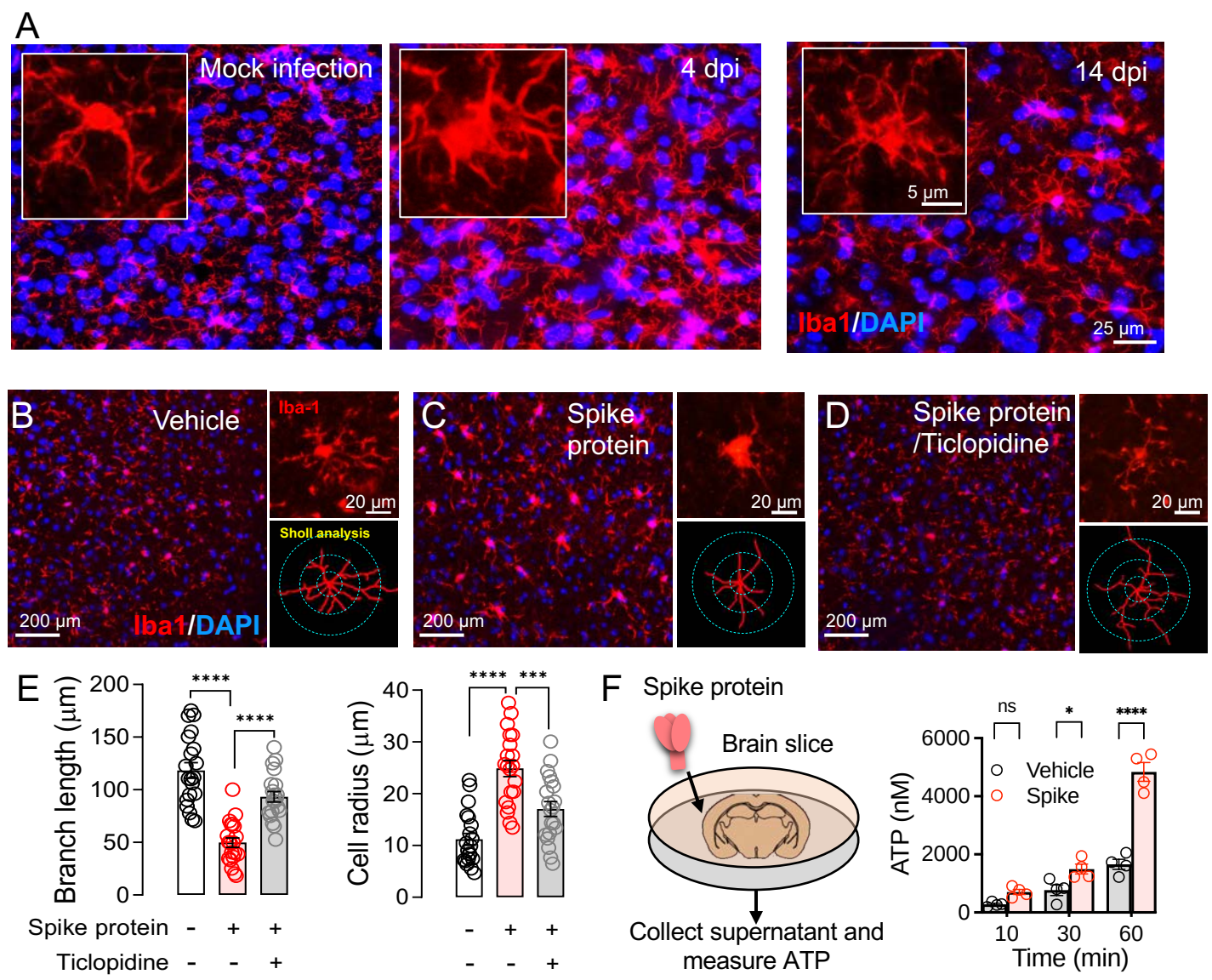

Figure. 6. Microglial Activation in Response to SARS-CoV-2 infection and B1.351 Spike Protein. (A) Dynamics of Microglial Activation Post-Infection in the Amygdala of Mice. Immunofluorescence staining for Iba1 highlights microglia in amygdala slices from mice at various time points following infection. An enlarged view of individual microglia provided to detail the changes in shape and morphology indicative of activation states. **(B-D)** Microglial response to perfusion with the spike protein. Immunostaining with Iba-1 illustrates microglial morphology in brain slices after a one-hour perfusion with the (B) vehicle or (C) spike protein (S1+S2, B.1.351, β variant, 167 ng/ml), and (D) spike protein following a 30-minute pretreatment with 50 µM Ticlopidine, a P2Y12R antagonist. The series showcases the microglial response to the spike protein, with additional magnified images highlighting the individual microglia and their morphological analysis using Sholl analysis, presented to the right of each panel. **(E)** Comparison of microglial activation assessed by Sholl analysis, which measures the total branch length and radius of cell area. Statistical significance: ****$p < 0.0001$, ***$p = 0.0006$, determined by one-way ANOVA with Tukey's post hoc multiple comparisons. The analysis includes data from 30 cells across 4 slices in each group. **(F)** Quantification of ATP release. Brain slices were incubated in cold PBS with either vehicle or spike protein (167 ng/ml). Supernatants were collected at 10, 30, and 60 minutes post-incubation. The amount of ATP released into the supernatant was quantified. Each dot is an independent brain slice and represents the mean of 2 technical replicates. Statistical significance: *$p = 0.0374$, ****$p < 0.0001$, determined by two-way ANOVA. Data are presented as mean ± SEM.

Figure. 7

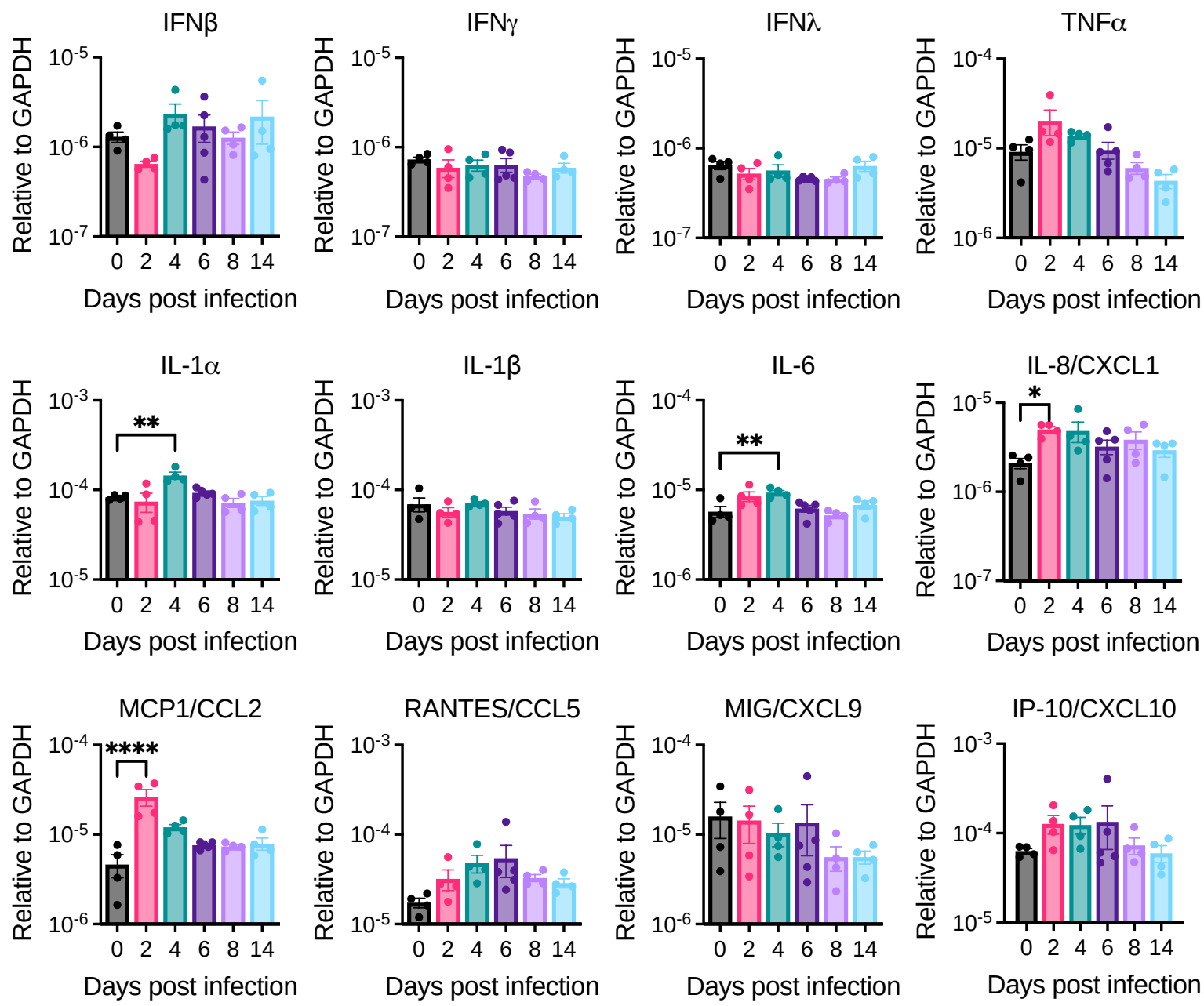

Figure. 7. Cytokines and Chemokines Induced in the Brain of SARS-CoV-2-Infected Mice. Brains of C57BL/6 mice intranasally infected with 10^4 PFU of SARS2-N501Y$_{MA30}$ were harvested at indicated days post-infection. Cytokine and chemokine transcripts were measured by quantitative real-time PCR (qRT-PCR) analyzing total RNA extracted from mock-infected (0 dpi) and infected young C57BL/6 mice. Each brain was collected from one individual mouse. Mock (0 dpi), 2, 4, 8, 14 dpi: n=4; 6 dpi: n=5. The levels of transcripts were normalized to GAPDH and presented as 2^-ΔCT. Statistical significance: *$p < 0.05$, **$p < 0.01$, ****$p < 0.0001$, determined by ordinary one-way ANOVA. Data are presented as mean ± SEM.

Figure. 8

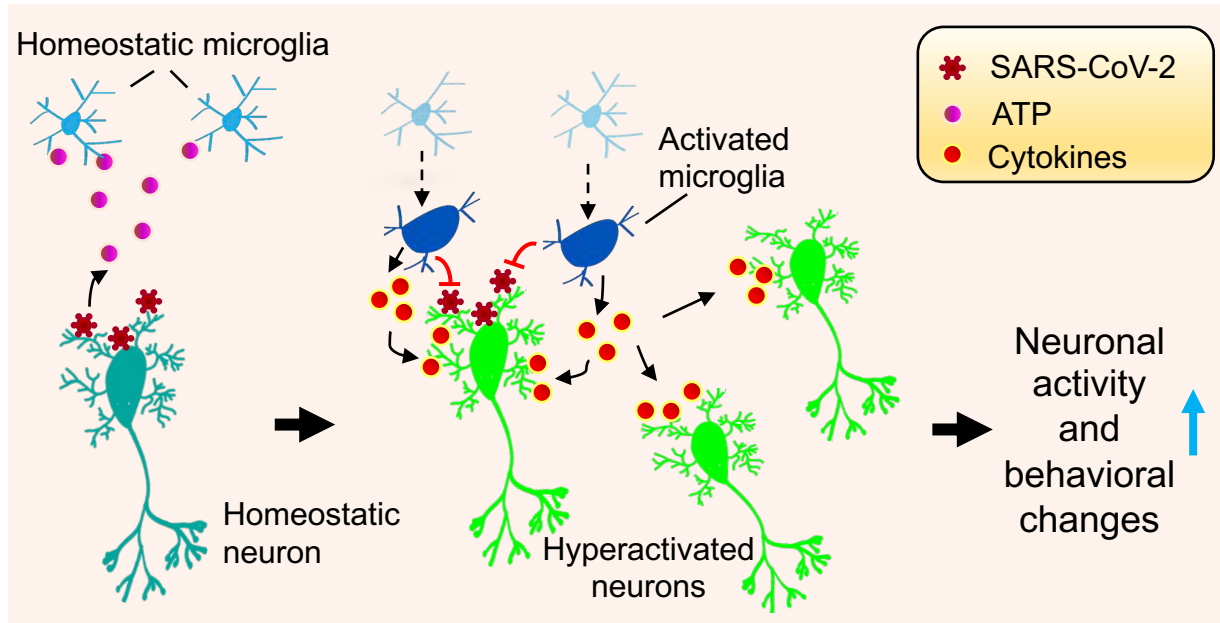

Figure. 8. Modeling Neurotropism-induced Behavioral Changes by SARS2-N501Y$_{MA30}$. This schematic illustrates the potential mechanism of SARS-CoV-2 targeting neurons, prompting ATP release, which in turn recruits and activates microglia. The ensuing cascade of microglial response and pro-inflammatory cytokine production is hypothesized to amplify neuronal activity, potentially altering defensive behaviors associated with anxiety and depression.

Supplementary Figure. 1

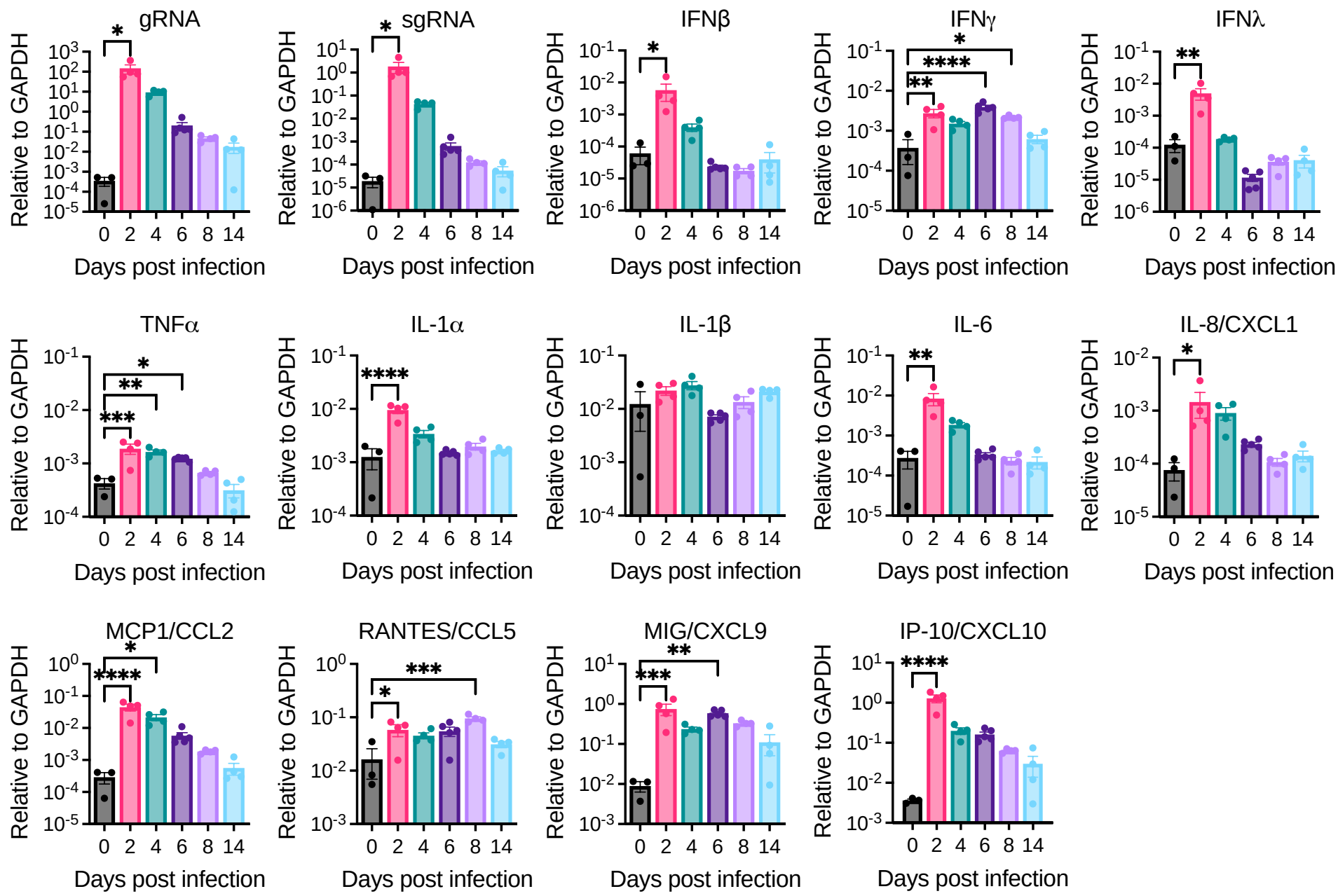

Supplemental Figure 1. SARS2-N501Y$_{MA30}$ Virus RNA Replication and Host Immune Responses in the Lungs. Total RNA was extracted from lungs collected from C57BL/6 mice (n=3 to 5), intranasally infected with 10^4 PFU of SARS2-N501Y$_{MA30}$ at designated days post-infection. Viral RNA, as well as host cytokine and chemokine transcripts, were quantified using quantitative real-time polymerase chain reaction (qRT-PCR). Viral gRNA or sgRNA CT values from mock-infected tissues (0 dpi) exceeded 35. Transcript levels were normalized to GAPDH and presented as 2^-ΔCT. Statistical significance was assessed using ordinary one-way ANOVA, with significance levels indicated as follows: *p < 0.05, **p < 0.01, ***p < 0.001, ****p < 0.0001. Data are presented as mean ± SEM.

Supplementary Figure. 2

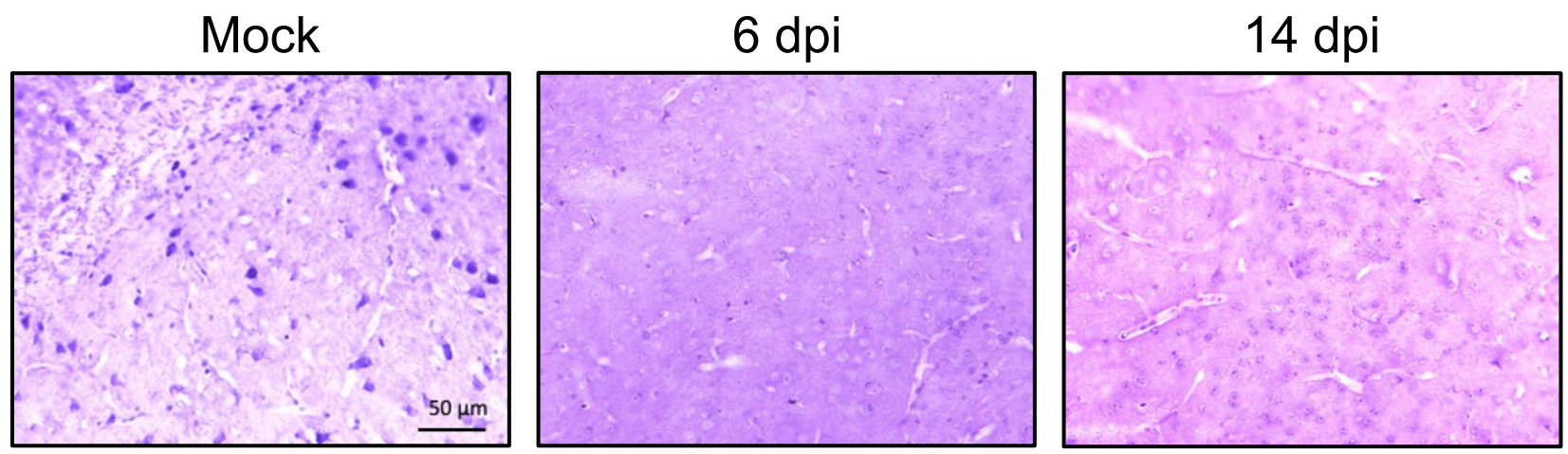

Supplemental Figure 2. Brain Histopathology after Mock and SARS2-N501Y$_{MA30}$ Infection. The representative images of brain tissue sections were stained with hematoxylin and eosin (H&E) at indicated days following either mock or SARS-CoV-2 infection. Scale bar: 50 µm

Supplementary Figure. 3

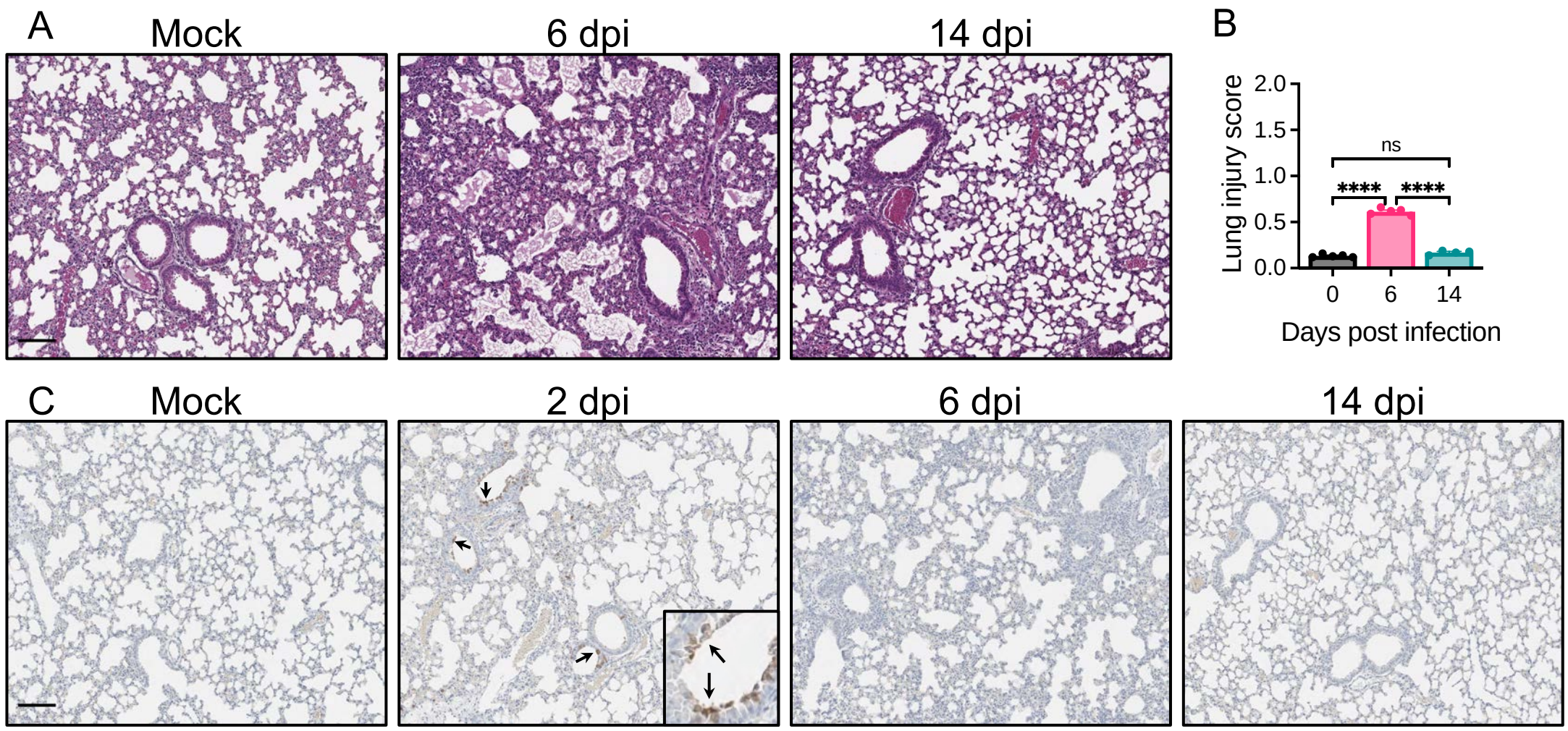

Supplemental Figure 3. Lung Pathology and Immunohistochemistry of Viral Protein. (A) Lung sections from mice infected with SARS2-N501Y$_{MA30}$ (n=5 for mock infection and for 6 dpi; n=4 for 14 dpi) underwent H&E staining. **(B)** Acute lung injury severity was assessed blindly following ATS guidelines (32), with 0 for no injury, 1 for mild to moderate injury, and 2 for severe injury. ****$p < 0.0001$. Scale bars: 100 μm. Data are shown as mean ± SEM. **(C)** Lung Tissue Immunohistochemistry revealing SARS-CoV-2 N protein (black arrows). Representative images show the presence of SARS-CoV-2 N protein (indicated by black arrows) at specified days post-infection. Scale bar: 100 μm.

Supplementary Figure. 4

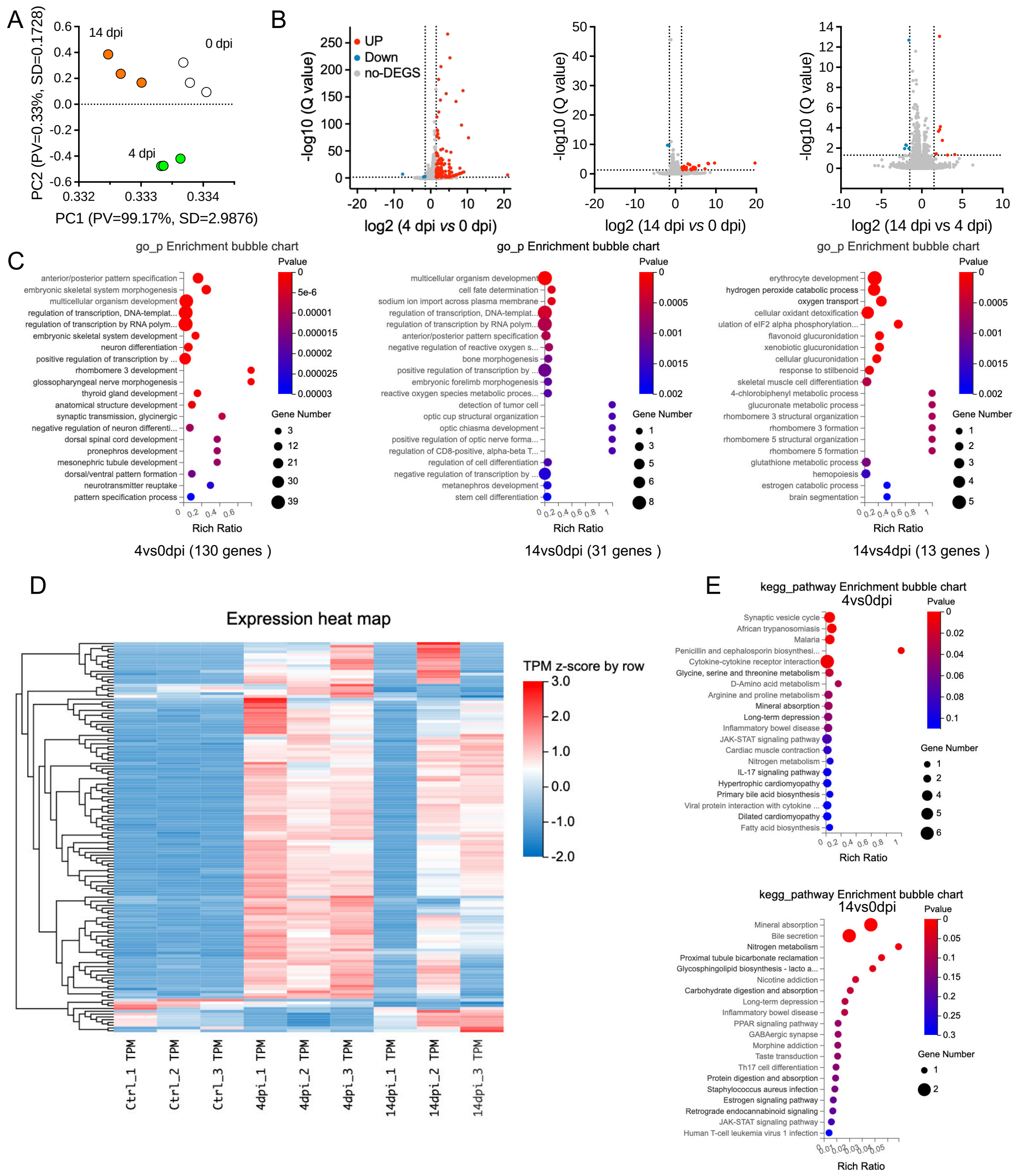

Supplemental Figure 4. Transcriptomic Profile Overview in SARS2-N501Y$_{MA30}$ infected mouse brains. (A) Principal Component Analysis (PCA) of transcriptome profiles comparing mock-infected brains (0dpi) with those at 4 and 14 days post-infection. **(B)** Volcano Plot Analysis: The x-axis denotes log2-transformed fold changes, and y-axis indicates -log10-transformed significant values. (Thresholds set at |log2fold| ≥ 1.5, Q value ≤ 0.05) **(C)** Gene Ontology (GO) Enrichment Analysis of DEGs across groups. **(D)** Heatmap visualization of 140 DEGs identified post-infection. **(E)** Kyoto Encyclopedia of Genes and Genomes (KEGG) Pathway Analysis comparing groups at 4dpi vs 0dpi, 14dpi vs 0dpi.

S1 Table

Gene	Forward Primer	Reverse Primer
2019-nCoV_N1	GACCCCAAAATCAGCGAAAT	TCTGGT TACTGCCAGTTGAATCTG
SARS-CoV-2 sgRNA for E	CGATCTCTTGTAGATCTGTTCTC	ATATTGCAGCAGTACGCACACA
mGAPDH	AACAGCAACTCCCACTCTTC	CCTGTTGCTGTAGCCGTATT
mIFNβ	TCAGAATGAGTGGTGGTTGC	GACCTTTCAAATGCAGTAGATTCA
mIFNγ	CGGCACAGTCATTGAAAGCCTA	GTTGCTGATGGCCTGATTGTC
mIFNλ	AGCTGCAGGTCCAAGAGCG	GGTGGTCAGGGCTGAGTCATT
mTNFα	GAACTGGCAGAAGAGGCACT	AGGGTCTGGGCCATAGAACT
mIL1a	CGCTTGAGTCGGCAAAGAAAT	ACAAACTGATCTGTGCAAGTCTC
mIL-1b	ACTGTTTCTAATGCCTTCCC	ATGGTTTCTTGTGACCCTGA
mIL-6	GAGGATACCACTCCCAACAGAC C	AAGTGCATCATCGTTGTTCATACA
mIL-8	CACCTCAAGAACATCCAGAGCT	CAAGCAGAACTGAACTACCATCG
mCCL2	CTTCTGGGCCTGCTGTTCA	CCAGCCTACTCATTGGGATCA
mCCL5	AGATCTCTGCAGCTGCCCTCA	GGAGCACTTGCTGCTGGTGTAG
mCXCL9	GCCATGAAGTCCGCTGTTCT	GGGTTCCTCGAACTCCACACT
mCXCL10	GCCGTCATTTTCTGCCTCAT	GCTTCCCTATGGCCCTCATT